# Constraining N₂O emissions since 1940 using firn air isotope measurements in both hemispheres

**M. Prokopiou[1], P. Martinerie[2], C. J. Sapart[1,3], E. Witrant[4], G. Monteil[1,5], K. Ishijima[6], S. Bernard[2], J. Kaiser[7], I. Levin[8], T. Blunier[9], D. Etheridge[10], E. Dlugokencky[11], R. S. W. van de Wal[1], T. Röckmann[1]**

[1] Institute for Marine and Atmospheric research Utrecht, Utrecht, The Netherlands

[2] University of Grenoble Alpes/CNRS, IRD, IGE, F-38000 Grenoble, France

[3] Laboratoire de Glaciologie, ULB, Brussels, Belgium

[4] University of Grenoble Alpes/CNRS, GIPSA-lab, F-38000 Grenoble, France

[5] Department of Physical Geography and Ecosystem Science, Lund University, Lund, Sweden

[6] National Institute of Polar Research, Tokyo, Japan

[7] Centre for Ocean and Atmospheric Sciences, School of Environmental Sciences, University of East Anglia, Norwich, United Kingdom

[8] Institute of Environmental Physics, Heidelberg University, Germany

[9] Centre for Ice and Climate, Niels Bohr Institute, Copenhagen, Denmark

[10] CSIRO Marine and Atmospheric Research, Victoria, Australia

[11] NOAA Earth System Research Laboratory, Boulder, Colorado, USA

## Abstract

N₂O is currently the 3$^{rd}$ most important anthropogenic greenhouse gas in terms of radiative forcing and its atmospheric mole fraction is rising steadily. To quantify the growth rate and its causes over the past decades, we performed a multi-site reconstruction of the atmospheric N₂O mole fraction and isotopic composition using new and previously published firn air data collected from Greenland and Antarctica in combination with a firn diffusion and densification model. The multi-site reconstruction showed that while the global mean N₂O mole fraction increased from (290±1) nmol mol⁻¹ in 1940 to (322±1) nmol mol⁻¹ in 2008 the isotopic composition of atmospheric N₂O decreased by (−2.2±0.2) ‰ for $\delta^{15}N^{av}$, (−1.0±0.3) ‰ for $\delta^{18}O$, (−1.3±0.6) ‰ for $\delta^{15}N^{\alpha}$, and (−2.8±0.6) ‰ for $\delta^{15}N^{\beta}$ over the same period. The detailed temporal evolution of the mole fraction and isotopic composition derived from the firn air model was then used in a two-box atmospheric model (comprising a stratospheric and

a tropospheric box) to infer changes in the isotopic source signature over time. The precise value of the source strength depends on the choice of the N$_2$O lifetime, which we choose to fix at 123 a. The average isotopic composition over the investigated period is $\delta^{15}N^{av}$ = ($-7.6\pm0.8$) ‰ (vs. air-N$_2$) $\delta^{18}O$ = ($32.2\pm0.2$) ‰ (vs. VSMOW) for $\delta^{18}O$, $\delta^{15}N^{\alpha}$ = ($-3.0\pm1.9$) ‰ and $\delta^{15}N^{\beta}$ = ($-11.7\pm2.3$) ‰. $\delta^{15}N^{av}$ and $\delta^{15}N^{\beta}$ show some temporal variability while for the other signatures the error bars of the reconstruction are too large to retrieve reliable temporal changes. Possible processes that may explain trends in $^{15}$N are discussed. The $^{15}$N site-preference (= $\delta^{15}N^{\alpha}$ − $\delta^{15}N^{\beta}$) provides evidence for a shift in emissions from denitrification to nitrification, although the uncertainty envelopes are large.

## 1 Introduction

The rise of nitrous oxide (N$_2$O) since pre-industrial times contributes significantly to radiative forcing (Forster et al., 2007). Over the past four decades, the N$_2$O mole fraction has increased by 0.25 % per year, reaching 324 nmol mol$^{-1}$ in 2011 (Ciais et al., 2013). Therefore, the understanding of the biogeochemical cycle of N$_2$O is important for a reliable assessment of future climate change. In addition, the destruction of N$_2$O in the stratosphere provides an important source of nitrogen oxides (NO$_x$), which contribute to stratospheric ozone depletion (Ravishankara et al., 2009; Crutzen, 1979; McElroy et al., 1971).

Natural sources of N$_2$O are microbial processes in soils and oceans, which produce N$_2$O during nitrification and denitrification (Bouwman et al., 2013; Loescher et al., 2012; Santoro et al., 2011; Galloway et al., 2004; Pérez et al., 2001; Yung and Miller, 1997; Kim and Craig, 1993). The increase of N$_2$O since pre-industrial times (hereafter referred to as "anthropogenic" increase) has been attributed largely to increased microbial production, resulting from the increased use of nitrogen fertilizers in agriculture. Industry (especially nylon production) and fossil fuel combustion present a smaller contribution to the anthropogenic source (Davidson, 2009; Kroeze et al., 1999; Mosier et al., 1998). N$_2$O is primarily destroyed in the stratosphere via UV photolysis (90 %) and reactions with excited oxygen atoms (10 %) (Minschwaner et al., 1993), with a minor N$_2$O fraction removed by surface sinks (Syakila, 2010).

Estimates of the total N$_2$O source strength from various bottom-up and top-down studies suggest a mean value of roughly 17 Tg a$^{-1}$ N equivalents at present. However, the range in both approaches is large, especially for bottom-up estimates, which range between 8.5 and 27.7 Tg a$^{-1}$ N, whereas top-down estimates range between 15.8 and 18.4 Tg a$^{-1}$ N (Potter et

62  al., 2011 and references therein). Besides the total source strength, the contributions of
63  individual source processes are also poorly constrained. Due to the long steady-state lifetime
64  of $N_2O$ in the atmosphere (123 a; SPARC Lifetimes Report 2013), temporal and spatial
65  gradients are small, making it difficult to resolve localised sources.

66  Measurements of the isotopic composition of $N_2O$ may help to constrain the atmospheric $N_2O$
67  budget. The $N_2O$ molecule is linear (NNO) and the two N atoms are chemically
68  distinguishable as a consequence they tend to attain different isotopic compositions. Beyond
69  oxygen ($\delta^{18}O$, $\delta^{17}O$) and average $\delta^{15}N^{av}$ ("bulk") signatures, $N_2O$ also displays site specific
70  $^{15}N$ isotopic information. Site preference ($\delta^{15}N^{sp}$) is defined as the difference in $\delta^{15}N^{av}$
71  between the central (2, μ or α) and terminal position (1, τ or β) of N atoms in $N_2O$ (Kaiser,
72  2002; Brenninkmeijer and Röckmann, 2000; Yoshida and Toyoda, 1999), i.e. $\delta^{15}N^{sp} = \delta^{15}N^{\alpha} -$
73  $\delta^{15}N^{\beta}$. For consistency with many recent publications in the field, we here adopt the
74  nomenclature from Yoshida and Toyoda (1999), α and β, for the two positions.

75  The different sources and sinks of $N_2O$ are associated with characteristic fractionation
76  processes leading to different isotope ratios. For example, microbial sources emit $N_2O$ that is
77  depleted in $^{15}N$ and $^{18}O$ relative to the tropospheric background. $N_2O$ that returns from the
78  stratosphere after partial photochemical removal is enriched in both heavy isotopes (Yoshida
79  and Toyoda, 2000; Rahn and Wahlen, 1997; Yung and Miller, 1997; Kim & Craig, 1993).
80  Stratospheric $N_2O$ also has a high $^{15}N$ site-preference compared to tropospheric $N_2O$. The
81  observed enrichment is caused by kinetic isotope fractionation in the stratospheric sink
82  reactions (Kaiser et al., 2006; 2002; Park et al., 2004; Röckmann et al., 2001; Yoshida and
83  Toyoda, 2000; Rahn et al., 1998).

84  The multi-isotope signature of $N_2O$ adds useful constraints on its budget. In particular, when
85  the isotopic composition of tropospheric $N_2O$ is combined with the fractionation during its
86  removal in the stratosphere, the isotopic composition of the global average source can be
87  determined (Ishijima et al., 2007; Bernard et al., 2006; Röckmann et al., 2003; Kim and Craig,
88  1993).

89  The temporal variations of the $N_2O$ isotopic composition are difficult to quantify on a short
90  timescale because of its long residence time in the atmosphere. Longer time scales can be
91  reconstructed by using air trapped in Arctic and Antarctic firn and ice which provides a
92  natural archive of past atmospheric composition. The firn phase is the intermediate stage
93  between snow and glacial ice, which constitutes the upper 40-120 m of the accumulation zone

of ice sheets. Within the firn, air exchanges relatively freely in the upper layers and with the overlying atmosphere (convective zone). With increasing depth the air pores shrink in size due to firn compaction, and air mixes primarily via slow diffusion in the diffusive zone. At densities larger than $\approx 815$ kg m$^{-3}$, air is permanently trapped in closed bubbles in the ice and totally isolated from the atmosphere. The precise age range of air that can be retrieved from polar firn between the surface and bubble close-off depends on site specific characteristics like temperature, accumulation rate and porosity and typically ranges from several decades to 120 years.

For $N_2O$, a number of studies have reported isotope measurements from different Arctic and Antarctic firn drilling sites showing a steady decrease of the heavy isotope content of $N_2O$ over the past decades (Park et al., 2012; Ishijima et al., 2007; Bernard et al., 2006; Röckmann et al., 2003; Sowers et al., 2002). A more recent study by Park et al. (2012) attempted to reconstruct the long-term trends in $N_2O$ isotopic compositions and its seasonal cycles to further distinguish between the influence of the stratospheric sink and the oceanic source at Cape Grim, Tasmania, demonstrating that isotope measurements can help in the attribution and quantification of surface sources in general.

Taking into account the long atmospheric lifetime of $N_2O$ and the fact that both hemispheres are well mixed on annual timescales, it is reasonable to assume that the results from these studies are representative for the global scale. However care needs to be taken because small differences in the diffusivity profiles of the firn column lead to large effect on the isotope signature (Buizert et al., 2012). Interestingly, for atmospheric methane ($CH_4$), another important greenhouse gas, a recent multi-site analysis of its carbon isotopic composition showed large differences among reconstructions from different sites (Sapart et al., 2013). In particular, firn fractionation effects related to diffusion and gravitational separation and their implementation in models (Buizert et al., 2012) have large effects on the reconstructed signals. Small differences in the diffusivity profiles of the firn column lead to large effects on the isotope signatures. Therefore, more robust results may be obtained by combining isotope information from a number of different sites in a multi-site reconstruction, including a critical evaluation of diffusivity profiles.

Here we combine new $N_2O$ isotope measurements from the NEEM site in Greenland with previously published firn air $N_2O$ isotope records from 4 different sites from Greenland and Antarctica to reconstruct records of the $N_2O$ isotopic composition over the last 70 years. We

126 use the multi-gas firn transport model developed by the Laboratoire de Glaciologie et

127 Géophysique de l'Environnement and Grenoble Image Parole Signal Automatique (LGGE-

128 GIPSA) to obtain an atmospheric scenario that is constrained by and consistent with all

129 individual sites (Allin et al., 2015; Witrant et al., 2012; Wang et al., 2012; Rommelaere et al.,

130 1997). We then use an isotope mass balance model to infer the changes in the isotopic

131 signature of the $N_2O$ source over time to investigate possible changes in the source mix.

132 **2    Materials and Methods**

133 **2.1    Firn air Sampling**

134 New firn air samples added in this study to the total dataset were collected in 2008 and 2009

135 during the firn campaign (Buizert et al., 2011) as part of the North Eemian Ice Drilling

136 programme (NEEM) in Greenland (77.45º N 51.06º W). These data are combined with

137 existing firn air data from four other sites. Information on the locations is provided in Table 1.

138 The firn air collection procedure is described in detail by Schwander et al. (1993). Here a

139 brief description is presented. Essentially a borehole is drilled in the firn to a certain depth and

140 then the firn air sampling device is inserted into the borehole. The device consists of a

141 bladder, a purge line and a sample line. When the sampling device reaches the desired depth

142 the bladder is inflated to seal the firn hole and isolate the air below the bladder from the

143 overlying atmosphere, and air is pumped out from the pore space below the bladder.

144 Continuous online $CO_2$ concentration measurements are performed to verify that no

145 contamination with contemporary air occurs during the extraction procedure. After the

146 contaminating air has been pumped away, firn air is collected in stainless steel, glass or

147 aluminium containers.

148 **2.2    $N_2O$ isotope analysis**

149 The firn air samples from NEEM are analyzed for $N_2O$ isotopocules at the Institute for

150 Marine and Atmospheric research Utrecht (IMAU). The $N_2O$ mole fraction and isotopic

151 composition are measured using continuous flow isotope ratio mass spectrometry (IRMS).

152 The method is described in detail by Röckmann et al. (2003b). Here only a brief summary is

153 given. The firn air sample (333 mL) is introduced into the analytical system at a flow rate of

154 50 mL/min for 400 s. After $CO_2$ is removed chemically over Ascarite, $N_2O$ and other

155 condensable substances are cryogenically preconcentrated. After cryo-focusing the sample the

156   remaining traces of $CO_2$ and other contaminants are removed on a capillary GC column

157   (PoraPlot Q, 0.32 mm i.d., 25 m). The column is separated into a pre-column and an

158   analytical column. This set-up eliminates interferences from other atmospheric compounds

159   that have much longer retention times. Finally the sample is transferred to the IRMS via an

160   open split interface. For the new NEEM samples reported here, each firn air sample has been

161   measured five times. Before and after each sample we measured five aliquots of air from a

162   reference cylinder with known isotopic composition and mole fraction for calibration

163   purposes.

164   $\delta^{15}N^{av}$ values are reported with respect to Air-$N_2$ while $\delta^{18}O$ refers to Vienna Standard Mean

165   Ocean Water (VSMOW). As laboratory reference gas we used an atmospheric air sample with

166   an $N_2O$ mole fraction of 318 nmol mol$^{-1}$ and $\delta$ values of (6.4±0.2) ‰ for $\delta^{15}N^{av}$ vs. Air-$N_2$,

167   (44.9±0.4) ‰ for $\delta^{18}O$ vs. VSMOW. The intramolecular $\delta^{15}N^{av}$ values of the air standard are

168   $\delta^{15}N^{\alpha}$ = (15.4±1.2) ‰ and $\delta^{15}N^{\beta}$ = (–2.7±1.2) ‰. The calibration of the intramolecular

169   distribution follows Toyoda and Yoshida (1999). Typically the 1σ standard deviations of

170   replicate sample measurements are 0.1 ‰ for $\delta^{15}N^{av}$, 0.2 ‰ for $\delta^{18}O$ and 0.3 ‰ for $\delta^{15}N^{\alpha}$ and

171   $\delta^{15}N^{\beta}$.

## 2.3   Modelling trace gas transport in firn

173   In firn air, the interstitial gas is not yet isolated in closed-off bubbles, so diffusion processes

174   and gravitational separation alter mole fractions and isotope ratios over time. Thus, firn air

175   measurements cannot be used directly to derive the atmospheric history of trace gas

176   signatures. Over time, atmospheric compositional changes are propagated downwards into the

177   firn based on the diffusivity of the atmospheric constituent in question. Firn air diffusion

178   models take these effects into account and thereby allow reconstruction of changes in the

179   atmospheric composition from the firn profile.

180   In this study we use the LGGE-GIPSA firn air transport model to reconstruct the temporal

181   evolution of $N_2O$ mole fraction and isotopic composition from the measured firn profiles

182   (Allin et al., 2015; Witrant et al., 2012; Wang et al., 2012; Rommelaere et al., 1997).

183   In the "forward version" of LGGE-GIPSA, a physical transport model uses a historic

184   evolution of atmospheric $N_2O$ mole fractions to calculate the vertical profiles of mole

185   fractions in firn. For the isotopocules, further simulations are performed separately to

186   calculate their respective vertical profiles. Important parameters needed to constrain the

187    model are the site temperature, accumulation rate, depth of the convective layer and close-off

188    depth, together with profiles of firn density and effective diffusivity. The latter parameter is

189    determined as a function of depth for each firn-drilling site by modelling the mole fractions in

190    firn for trace gases with well known atmospheric histories (Buizert et al., 2012; Witrant et al.,

191    2012; Rommelaere et al., 1997; Trudinger et al., 1997). A multi-gas constrained inverse

192    method (Witrant et al., 2012) is used to calculate the effective diffusivity of each site for each

193    specific gas. It is noteworthy that diffusivity is not constrained equally well at all sites

194    because different sets of constraints (e.g. number of available reference gases) are used at

195    different sites and because of different depth resolutions.

196    A Green-function approach, as presented by Rommelaere et al. (1997) and used for

197    halocarbon trend reconstruction by Martinerie et al. (2009), with an extension for isotopic

198    ratios and revised to take into account the scarcity of the measurements (Allin et al., 2015;

199    Witrant and Martinerie, 2013; Wang et al., 2012) is used to assign a mean age and age

200    distribution to a certain depth.

201    Due to the long $N_2O$ residence time in the atmosphere, the global variability of the isotopic

202    composition of $N_2O$ is very small and no significant variations between individual

203    background locations have been detected so far (Kaiser et al., 2003). In particular, the isotope

204    ratio difference between northern and southern hemisphere tropospheric air is expected to be

205    only −0.06 ‰ (based on an interhemispheric mole fraction gradient of 1.2 nmol mol$^{-1}$ [Hirsch

206    et al. 2006] and isotope ratio difference of −15 ‰ between average source and average

207    tropospheric isotopic delta value). These differences are within the uncertainties of the firn air

208    measurements used here and therefore the data from the northern and southern hemisphere are

209    combined into a single dataset without including an interhemispheric gradient.

210    With the multi-site reconstruction method, we used the measurements from six firn air

211    drillings at five sites (NEEM-09, NEEM-EU-08, BKN-03, NGRIP-01$_{Bernard}$,  DC-99, DML-

212    98) to constrain our model and determine a set of atmospheric reconstructions that fits all

213    sites. Data from Ishijima et al. (2007) and Sowers et al. (2002) [NGRIP-01$_{Ishijima}$ and SP-01,

214    SP-95 respectively] were not included in our multi-site reconstruction because no data for

215    $\delta^{15}N^{\alpha}$ and $\delta^{15}N^{\beta}$ were published for those sites. These datasets were used for independent

216    validation of $\delta^{15}N^{av}$ and $\delta^{18}O$.

217    To quantify the isotope fractionation due to diffusion and gravitational settling within the firn,

218    a forward firn transport model simulation was carried out with a realistic $N_2O$ mole fraction

219    scenario (based on the Law Dome record, MacFarling Meure et al., 2006), but with a constant

220    isotopic $N_2O$ history. This allows determining the role of transport isotope fractionation

221    occurring in the firn, in the absence of isotopic changes in the atmosphere. The results are

222    used to subtract the firn fractionation effects from the measured signals, which can then be

223    used to assess the atmospheric history. Compared to the signal, the effect of firn fractionation

224    is minor for $\delta^{15}N^{av}$, but important for $\delta^{18}O$ especially at the lower accumulation rates in the

225    Southern Hemisphere (see Appendix A).

226    The deepest firn data from each site provide constraints furthest back in time and the oldest

227    air samples that are included in the inversion are from the DML-98 and DC-99, which extend

228    the reconstruction of atmospheric $N_2O$ back to the early 20th century (Röckmann et al., 2003).

229    At the same time, the correction for isotopic fractionation in firn is most uncertain for the

230    deepest samples, where strong differences between individual firn air models have been

231    reported (Buizert et al., 2012).

## 2.4    Scaling of different data sets

233    At present, no international reference materials for the isotopic composition of $N_2O$ exist.

234    Kaiser et al. (2003) and Toyoda et al. (1999) linked the isotopic composition of $N_2O$ in

235    tropospheric air to the international isotopes scales for nitrogen isotopes (Air-$N_2$) and oxygen

236    isotopes (either VSMOW or Air-$O_2$). Our measurements are linked to a standard gas cylinder

237    of tropospheric air with known $N_2O$ mole fraction and isotopic composition based on the

238    scale of Kaiser et al. (2003) for $\delta^{15}N^{av}$ and $\delta^{18}O$ values and Yoshida and Toyoda (1999) for

239    position dependent $^{15}N$ values. However, the reference air cylinder used for the calibration

240    was exhausted and had to be replaced three times over the years in which the different

241    measurement that we combine in this study were performed. Although the cylinders were

242    carefully compared, the long-time consistency of the isotope scale could not be guaranteed

243    because long-time isotope standards are not available. In fact, analysis of the data from the

244    convective zone for the different sites, show small but significant differences from the

245    temporal trends that are well established from previously published data from the German

246    Antarctic Georg von Neumayer station for 1990 to 2002 (Röckmann and Levin; 2005). The

247    linear trends reported in that paper are $(-0.040\pm0.003)$ ‰ a$^{-1}$ for $\delta^{15}N^{av}$, $(0.014\pm0.016)$ ‰ a$^{-1}$

248    for $\delta^{15}N^{\alpha}$, $(-0.064\pm0.016)$ ‰ a$^{-1}$ for $\delta^{15}N^{\beta}$ and $(-0.021\pm0.003)$ ‰ a$^{-1}$ for $\delta^{18}O$. Since they were

249    derived from direct air samples (unaffected by firn fractionation), these trends can be used as

250    a reference to re-scale the different firn air results from different dates. To do so, data from

251    the diffusive zone ($\rho < 815$ kg m$^{-3}$) for each individual site were scaled to one reference site,

252    DC-99, taking into account the temporal differences in sampling and the model-assigned

253    mean age of the firn air samples (see below). DC-99 was chosen as reference site because it

254    has most measurements in the diffusive zone. Also, the precision of these measurements was

255    high because high volume cylinders were available from which many measurements could be

256    performed and averaged. To test the sensitivity to the choice of reference site, we repeated the

257    re-scaling using NEEM-09 as reference, which generated almost identical results within

258    uncertainty bars (Appendix C).

259    The average difference between the samples from the diffusive zone at a given site and the

260    interpolated DC-99 results was compared to the expected temporal trend between the

261    sampling date of each station and DC-99, using the temporal trends established by Röckmann

262    and Levin (2005), as shown in the equations below. The effect of this scaling is that the

263    temporal trend in the past decade is effectively forced to follow the atmospheric

264    measurements at Neumayer station (Röckmann and Levin, 2005).

265    After re-scaling the firn isotopic data we detected some individual data points that clearly

266    deviated from the general trends. These were considered outliers, because they exceeded the

267    $2\sigma$ error, and were removed from the dataset. All of these values are site-specific $^{15}$N values,

268    specifically the following, were excluded: NEEM-EU-08 hole depth $-4.9$ m, $-34.72$ m, $-$

269    61.95 m and $-74.5$ m, and NEEM-09 hole depth 1.0 m, 0.2 m and $-69.4$ m.

270    The mole fraction data that can be obtained from the NEEM air isotope measurements were

271    substituted with more precise measurements of N$_2$O mole fraction by the Commonwealth

272    Scientific and Industrial Research Organisation (CSIRO) the Institute of Environmental

273    Physics, University of Heidelberg (IUP), the Centre of Ice and Climate, University of

274    Copenhagen (CIC) and National Oceanic and Atmospheric Administration (NOAA). In this

275    way we combine all available N$_2$O mole fraction data narrow the uncertainty envelope but do

276    not affect the trend.

277    The mole fraction data were scaled to the most recent international scale, NOAA-2006A from

278    the CSIRO scale or the NOAA-2000 scale. Conversion of the NOAA-2000 data to the

279    NOAA-2006A scale is done using a conversion factor available by National Oceanic and

280    Atmospheric                     Administration                    (NOAA)

281    (http://www.esrl.noaa.gov/gmd/ccl/scales/N2O_scale.html). Converting from the CSIRO to

282 the NOAA-2006A scale, though, requires the reference cylinder details, which were not
283 available. Instead we used a trend scenario, based on the CSIRO atmospheric scale combined
284 with Law Dome data and assuming a constant interhemispheric gradient. This trend scenario
285 was then compared with the data provided on NOAA-2006A scale, and a polynomial fit was
286 generated, which was then used to convert the data to the NOAA-2006A scale. All results
287 presented in the next section are based on the scaling procedure and removal of the outliers as
288 described above (Appendix B).

## 289 2.5 Global $N_2O$ (isotope) budget calculations

290 The tropospheric budget is controlled by $N_2O$ emissions from natural and anthropogenic
291 sources at the surface and by the exchange between troposphere and stratosphere. A simple
292 two-box model is used to quantitatively understand the emissions and the budget changes of
293 $N_2O$. The model consists of a tropospheric $N_2O$ reservoir (index T) into which $N_2O$ is emitted
294 from natural ($E_{nat}$) and anthropogenic ($E_{anth}$) sources. $N_2O$ is then transported to the
295 stratosphere (index S) where part of it is destroyed by photochemical reactions (L), and the
296 remainder returns from the stratosphere to the troposphere ($F_{exch}$).

297 The change in the tropospheric $N_2O$ reservoir is given by the following mass balance
298 equations (Allin et al, 2015):

$$299 \quad n_T \frac{d\chi_T}{dt} = E_{nat} + E_{anth} - F_{exch}(\chi_T - \chi_S) \tag{1}$$

$$300 \quad n_S \frac{d\chi_S}{dt} = F_{exch}(\chi_T - \chi_S) - L \tag{2}$$

301 where $n$ is the amount of air (85 % for troposphere and 15 % for stratosphere) and $\chi_S$ and $\chi_T$
302 are the mole fractions of $N_2O$ in the stratosphere and troposphere respectively. Annual fluxes
303 between the two reservoirs, $F_{exch}$, are calculated based on previous estimates (Appenzeller et
304 al., 1996; Holton et al., 1990) and given in Table 3. The loss due to stratospheric sink is
305 determined by:

$$306 \quad L = \frac{n_T\chi_T + n_S\chi_S}{\tau} \tag{3}$$

307 where $\tau$ is the atmospheric lifetime which we choose to fix at 123 a.

308 The isotopic budgets are calculated by simply multiplying the reservoir sizes with the
309 corresponding $\delta$ values of the different flux terms:

310 $\quad n_T \dfrac{d\chi_T \delta_T}{dt} = E_{nat}\delta_{nat} + E_{anth}\delta_{anth} + F_{exch}(\chi_S\delta_S - \chi_T\delta_T)$ $\qquad\qquad\qquad$ *(4)*

311 $\quad n_S \dfrac{d\chi_S \delta_S}{dt} = F_{exch}(\chi_T\delta_T - \chi_S\delta_S) - L\delta_L$ $\qquad\qquad\qquad\qquad\qquad$ *(5)*

312 Separating the l.h.s in two terms and substituting eq. 1 and 2 into eq. 4 and 5 yields the final

313 isotope equations:

314 $\quad n_T \dfrac{d\delta_T}{dt} = \dfrac{E_{nat}}{\chi_T}(\delta_{nat} - \delta_T) + \dfrac{E_{anth}}{\chi_T}(\delta_{anth} - \delta_T) + \dfrac{F_{exch}\chi_S}{\chi_T}(\delta_S - \delta_T)$ $\qquad\qquad$ *(6)*

315 $\quad n_S \dfrac{d\delta_S}{dt} = \dfrac{F_{exch}\chi_T}{\chi_S}(\delta_T - \delta_S) - \dfrac{L}{\chi_S}\varepsilon_L$ $\qquad\qquad\qquad\qquad\qquad$ *(7)*

316 where $\delta_T$ is either $\delta^{15}N^{av}$, $\delta^{18}O$, $\delta^{15}N^{\alpha}$, $\delta^{15}N^{\beta}$ from the multi-site reconstruction as shown

317 below. $\delta_{nat}$ and $\delta_{anth}$ is the isotopic composition of the natural and anthropogenic $N_2O$ source,

318 respectively (our target quantity). $\varepsilon_L$ is the isotopic fractionation factor associated with

319 stratospheric destruction.

320 $\delta_S$ is also not known, but can be calculated using the analogue from Röckmann et al. (2003)

321 by employing the observed apparent Rayleigh fractionation in the stratosphere ($\varepsilon_{app}$) (Table

322 3). Based on this, the relative isotope ratio difference between the stratosphere and the

323 troposphere can be calculated by:

324 $\quad \delta_S = \left[(\delta_T + 1)\left(\dfrac{\chi_S}{\chi_T}\right)^{\varepsilon_{app}} - 1\right]$ $\qquad\qquad\qquad\qquad\qquad\qquad$ *(8)*

325 Here, we used the average $\varepsilon_{app}$ of all lowermost stratospheric measurements from Kaiser et al.

326 (2006) (Table 3). Note that slightly different fractionations $\varepsilon_{app}$ have been used in previous

327 studies by Rahn and Wahlen (2000), Röckmann et al. (2001) and Park et al. (2012; 2004). The

328 sensitivity of the results to these differences will be examined below.

329 Furthermore we assume that the $N_2O$ lifetime and $\varepsilon_{app}$ remained constant from pre-industrial

330 time to 2008, thus the annual sink strength can be scaled down from its current value at $\chi_T =$

331 322 nmol mol$^{-1}$ to the pre-industrial level of $\chi_{T,pi} = 270$ nmol mol$^{-1}$ and the relative enrichment

332 of stratospheric $N_2O$ relative to tropospheric $N_2O$ described by Eq. 8 remains constant over

333 time. The effect of changing the $N_2O$ lifetime is also examined below.

334 Our model approach assumes that during the pre-industrial period only natural emissions

335 occurred without any anthropogenic input. After the industrialization ($\approx 1750$) any increase in

336    the emissions is considered to be due to anthropogenic input while natural emissions remain

337    constant. Hence, the temporal change in isotopic composition is formally due to the increase

338    in one single "anthropogenic" source only, which may in reality also contain a natural

339    component.

340    **2.6   Uncertainty estimation using random scenarios**

341    The precision of the calculated $N_2O$ emissions ($E_{nat}$, $E_{anth}$) depends primarily on the precision

342    of the atmospheric reconstruction of the $N_2O$ mole fraction ($\chi_T$). However, taking random

343    histories within the uncertainty envelope provided by the firn air reconstruction is not

344    adequate to quantify the uncertainty of the atmospheric $N_2O$ reconstruction: the year-to-year

345    variability of $N_2O$ is constrained by the $N_2O$ lifetime in the troposphere. Possible realistic

346    $N_2O$ scenarios are scenarios that are within the confidence intervals provided by the

347    atmospheric reconstructions, and that have realistic year-to-year variability.

348    Mathematically, this can be represented by an uncertainty variance covariance matrix **B**,

349    where the diagonal elements (variances) are the yearly uncertainties on the atmospheric $N_2O$

350    mole fractions, and the off-diagonals are the covariances of the uncertainties of different

351    years. The covariance between the uncertainty on the reconstruction in one year $i$ and the

352    uncertainty in another year $j$ is defined as:

353    $cov(i,j) = r_{i,j}\sigma_i\sigma_j$                                                             *(9)*

354    $r_{i,j} = f(|i\text{-}j|)$                                                                        *(10)*

355    The correlation ($r_{i,j}$) is maximum between two consecutive years, and decreases as the time

356    difference increases.

357    We generated an ensemble of 50 random realistic $N_2O$ scenarios within the uncertainty

358    envelope of the firn atmospheric $N_2O$ reconstruction constrained by the covariance matrix **B**.

359    For each of these atmospheric $N_2O$ scenarios, we calculated the corresponding $N_2O$ emission

360    time series. The range of emissions from these scenarios then provides a realistic estimate for

361    the uncertainty in $N_2O$ emissions.

362    We carried out the same analysis for the different $N_2O$ isotopocules: for each isotopocule ($\delta$

363    value), we generated a covariance matrix $\mathbf{B}^{\delta}$, constrained by the uncertainty ranges provided

364    by the atmospheric reconstructions and the correlation coefficients defined in Eq.9 and Eq.10

365  to generate a set of 50 random scenarios within the uncertainty envelopes. For each of these

366  random scenarios, we calculated the corresponding source signature scenario and the range in

367  the results provides an uncertainty estimate of the isotopic source signatures.

368  ## 3   Results

369  ### 3.1   Mean age

370  The mean age of $N_2O$ in air sampled from different depths in the firn for all datasets that are

371  used in this study is shown in Fig. 1. The strong change in the mean age gradient that is

372  clearly visible in each profile reflects the transition between the diffusive and bubble close-off

373  zones, which occurs at a specific depth and mean age for each site. Fig. 1 also shows that for

374  each site the few samples that are collected within the bubble close-off zone provide the

375  constraints for most of the reconstructed record (for instance, at BKN-03, 50 m depth is the

376  beginning of the bubble close-off zone). In addition to the mean age, the width of the age

377  spectrum also increases with depth. Therefore, the temporal resolution of signals that can be

378  reconstructed from the firn air measurements reduces with depth and approaches the one of

379  ice core samples towards the bottom of the bubble close-off zone.

380  The Greenland sites (NH) have similar meteorological and glaciological conditions (Table 1),

381  thus the differences between the mean age profiles in Fig. 1 are small. The Antarctic sites

382  (SH) show clear differences because the meteorological and glaciological variables differ

383  strongly from site to site. As a result the firn-ice transition is at a different depth for each

384  location (e.g., the firn-ice transition zone for DML-98 is located at about 73.5 m compared to

385  about 99.5 m at DC-99).

386  ### 3.2   Experimental results and multi-site reconstruction

387  Mole fraction and isotopic composition of $N_2O$ in firn air are presented versus depth of the

388  firn air sampling in the middle panels of Fig. 2 for the different sites. The mole fraction

389  decreases with depth in qualitative agreement with the known increase of $N_2O$ in the

390  atmosphere over time. In contrast, all isotope deltas slowly increase with depth in the upper

391  firn and show stronger heavy isotope enrichment in the close-off zone, both indicating heavy

392  isotope depletion in atmospheric $N_2O$ with time.

393  The atmospheric history that has been reconstructed from these firn datasets using the multi-

394  site inversion (using the data from NEEM-09, NEEM-EU-08, NGRIP-01$_{Bernard}$, BKN-03, DC-

13

395   99, DML-98) as described in section 2.4 is shown in the left column of Fig. 2. The solid line

396   shows the scenario that leads to the best fit with the firn data as shown in the middle panel,

397   and the dashed lines show the upper and lower range of possible scenarios that would still

398   produce an acceptable fit to the data within the uncertainty bars. Color-coded symbols show

399   data plotted at their respective mean age (as derived from the firn air model). When the best-

400   fit scenario is used as input for the forward firn air model for each individual site, the model

401   produces the vertical profiles that are shown as coloured lines together with the data in the

402   middle panels. For the sites that were included in the multi-site reconstruction, the firn

403   profiles based on the best-fit scenarios generally match the experimental data points well,

404   which is expected after a successful inversion procedure and with consistent data sets. The

405   right panels in Fig. 2 show the differences between these model results and the data. For the

406   data that were used in the multi-site inversion the model-data differences are generally very

407   small, although individual firn drilling sites in some cases show small systematic deviations,

408   in particular in the close-off zone. This means that when inversions would have been

409   performed on individual sites, the optimal reconstructions would be slightly different. Hence,

410   the advantage of the multi-site reconstruction is that the reconstructed scenario is constrained

411   by all sites and all sampling depths. Despite the small differences between individual sites, the

412   left panels show that all data fall within the uncertainty bars of the reconstructed scenario of

413   the inversion.

414   From 1940 to 2008 the total changes of the $\delta$ values of atmospheric $N_2O$ are $(-2.2\pm0.2)$ ‰ for

415   $\delta^{15}N^{av}$, $(-1.0\pm0.3)$ ‰ for $\delta^{18}O$, $(-1.3\pm0.6)$ ‰ for $\delta^{15}N^{\alpha}$ and $(-2.8\pm0.6)$ ‰ for $\delta^{15}N^{\beta}$

416   respectively (Fig. 2, left panels). The average linearized trends are $(-0.032\pm0.004)$ ‰ $a^{-1}$ for

417   $\delta^{15}N^{av}$, $(-0.014\pm0.008)$ ‰ $a^{-1}$ for $\delta^{18}O$, $(-0.019\pm0.015)$ ‰ $a^{-1}$ for $\delta^{15}N^{\alpha}$ and $(-0.041\pm0.020)$

418   ‰ $a^{-1}$ for $\delta^{15}N^{\beta}$. These overall trends are slightly lower compared to previous studies that

419   used only the data at individual sites (Ishijima et al., 2007; Bernard et al., 2006; Röckmann et

420   al., 2003; Sowers et al., 2002) and other studies that used data from the same period, which

421   were not used in the present study (Park et al., 2012). However, the differences are well

422   within the combined uncertainties. We note that comparisons of average linear trends can be

423   flawed when the firn air records have different length and the temporal profiles do not change

424   linearly (see below). Trends for $\delta^{15}N^{\alpha}$ are smaller in magnitude than for $\delta^{15}N^{\beta}$, while results

425   from Bernard et al. (2006) showed stronger changes for $\delta^{15}N^{\alpha}$ than for $\delta^{15}N^{\beta}$. However, in that

426   study the trends were largely determined from measurements on young ice core samples with

427   comparatively higher measurement errors and larger scatter.

428    Data from two sites were not included in the multi-site inversion and are used as independent

429    validation of the reconstructed scenarios. The data points from Ishijima et al. (2007) (NGRIP-

430    $01_{\text{Ishijima}}$, yellow) are within the range of scenarios reconstructed by the inverse model and

431    thus independently validate our results. The $\delta^{15}N^{av}$ and $\delta^{18}O$ data from Sowers et al. (2002)

432    (SP-01 in light blue and SP-95 in blue) however, agree only for the more recent atmospheric

433    history (Fig. 2, left panels). For mean ages before 1990 most of the points are outside the

434    uncertainty envelopes of the multi-site reconstruction. Inter-laboratory calibration differences

435    might be a possible explanation for the discrepancy, but the differences are not a systematic

436    shift, and they are larger than offsets among laboratories that were established in the past

437    (Sapart et al., 2011; Kaiser et al., 2003). In fact, the data reported by Sowers et al. (2002)

438    were actually measured in two different laboratories with good agreement. So measurement

439    flaws can be excluded. A possible origin of the difference could be based on the

440    reconstruction model. Because the uncertainties on the South Pole data are large, compared to

441    the other sites, the multi-site homogenization is more uncertain and less efficient (see

442    Appendix A and C, Fig. A1 and C1-C3).  Sampling uncertainty should also be taken into

443    consideration since when pumping firn air and filling the sampling flasks you could encounter

444    uncertainties (contamination, possible leak, fractionation, incomplete flask flushing etc). At

445    present though the discrepancy cannot be resolved.

446    To evaluate our scaling approach we repeated the multi-site reconstruction using the original

447    non re-scaled data and re-scaled them to NEEM-09 instead of DC-99 (see Appendix C). This

448    yielded similar results (within uncertainties) to the original reconstruction, thus results do not

449    depend on the choice of the site used for re-scaling. Without re-scaling, the overall change of

450    $N_2O$ mole fraction and isotopic composition remained the same, but an additional decadal

451    variability was introduced for $\delta^{15}N^{av}$, $\delta^{15}N^{\alpha}$ and $\delta^{15}N^{\beta}$. In addition to that, the uncertainty

452    envelopes doubled because of the scale inconsistencies. All scaling approaches produce

453    results that are consistent with our preferred scaling to DC-99 within the uncertainty

454    envelopes. We conclude that scaling removed the discrepancies that would cause larger

455    uncertainties if the original data were used instead, but the re-scaling does not introduce

456    artificial signals (see Appendix C).

457    The regularization of the inversion results using a rugosity factor introduces a free parameter,

458    which is chosen to eliminate overfitting of experimental uncertainties and which controls the

459    smoothness of the reconstruction. The value of this parameter is set based on a robust

460 generalized cross validation criterion, ensuring that the resolution obtained from the inverse
461 model is similar to the experimental data while taking into account the scarcity of the
462 measurements (Witrant and Martinerie, 2013). A sensitivity experiment where the weight of
463 the regularization term was increased by a factor 10 led to nearly linear tropospheric histories
464 within the uncertainty envelopes presented in Appendix C (Fig. C2). This combined with the
465 fact that straight lines can be drawn within the uncertainty envelopes of the reconstructed
466 scenarios and the sensitivity tests (see Appendix C) indicates that the isotopic trends are not
467 significantly different from straight lines within the current uncertainties.

### 3.3   Reconstruction of the $N_2O$ emission history

469 Fig. 3 shows the temporal evolution of the global $N_2O$ mole fraction as inferred from the
470 atmospheric reconstruction constrained only by the most precise NEEM data in the top panel,
471 and in the bottom panel the emission strength in Tg $a^{-1}$ N calculated with the mass balance
472 model (Section 2.5). The solid black line denotes the best estimate scenario, which is used as
473 input in the mass balance model. The magenta lines show the ensemble of random scenarios
474 generated to quantify the uncertainty of the emissions (see Section 2.6).

475 The increase in the $N_2O$ mole fraction of (32±1) nmol $mol^{-1}$ over the reconstruction period
476 can be explained in the mass balance model by a (4.4±1.7) Tg $a^{-1}$ N increase in the emissions
477 from 1940 to 2008. The emissions increased with an increasing trend until 1975, then the
478 annual increase continued, but at a slower rate up to 1990, and from then on the annual
479 emissions have stayed approximately constant or even decreased slightly. The minor increase
480 in the $N_2O$ mole fraction towards the end of the time series is likely not significant and does
481 influence our reconstructions. The corresponding changes in the mole fraction are difficult to
482 discern due to the long atmospheric lifetime of $N_2O$. On average, the annual growth rate from
483 1995 to 2008 period is 0.7 nmol $mol^{-1}$ $a^{-1}$, corresponding to average annual emissions of 3.5
484 Tg $a^{-1}$ N.

### 3.4   The temporal evolution of the $N_2O$ isotope signatures

486 The results from the isotope budget calculations are presented in Fig. 4. The left panels show
487 the atmospheric trends. The solid black lines represent the best-fit scenarios while the dashed
488 black lines represent the upper and lower uncertainty envelope of the firn air reconstructions.
489 The magenta lines represent 50 scenarios generated randomly within the reconstructed
490 uncertainty range, as described in section 2.6. The middle panels show the temporal changes

491    in the isotope signatures of the total $N_2O$ source, with their accompanied uncertainties, as

492    calculated from the atmospheric mass balance model (section 2.5). The total source is split

493    into an assumed constant "natural" and an increasing "anthropogenic" component and the

494    right panels show the isotopic evolution of the "anthropogenic" component.

495    Results show that the average $\delta^{15}N^{av}$ of the total $N_2O$ source, over the reconstruction period, is

496    (−7.6±0.6) ‰ where the uncertainty is calculated using the 1σ uncertainty from the scenarios

497    with respect to the mean value (magenta lines). There is no statistically significant long-term

498    trend, but a temporal variability is observed on the decadal scale that might mask this trend.

499    $\delta^{15}N^{av}$ first decreased from (−6.5±0.6) ‰ in 1940 to (−8.5±0.6) ‰ in 1965, then slowly

500    increased again to (−6.6±0.6) ‰ in 1985, followed by another decrease to (−8.5±0.6) ‰ in

501    2008. These oscillations originate from the slightly curved trends in the isotopic

502    reconstructions for $\delta^{15}N^{av}$ in Fig. 4 (left panels).

503    When the source is split into a constant natural and a varying anthropogenic component, the

504    variability is projected on the anthropogenic part and the temporal variations increase

505    accordingly. However, also the uncertainties increase substantially, because the differences

506    between the individual scenarios are attributed to only a small fraction of the total source.

507    The $\delta^{15}N^{av}$ signature of the anthropogenic source has an average value of (−18.2±2.6) ‰. It

508    initially increases (the small initial decrease is not significant) from (−21.5±2.6) ‰ in 1940 to

509    (−8.6±2.6) ‰ in 1990, when it starts to slowly decrease reaching (−15.4±2.6) ‰ in 2008.

510    During the early part of the reconstruction period before 1970, when the "anthropogenic"

511    contribution was only a small fraction of the total source, the uncertainty ranges of the source

512    signatures are larger. Therefore, the uncertainties for the early part were excluded when

513    calculating the 1σ uncertainties over the entire period from the generated scenarios. This

514    applies to all anthropogenic isotope signatures.

515    The budget calculations suggest an overall trend towards more enriched anthropogenic

516    emissions, but the uncertainties are large. Mathematically, this trend arises from the fact that

517    the isotope reconstructions yield relatively linear temporal isotope trends, whereas the source

518    strength increases in a strongly non-linear fashion (Fig. 4). In the beginning of the record a

519    small increase in the source strength needs to produce a certain absolute isotope shift, whereas

520    a smaller increase in the source strength is needed during later years to cause a similar isotope

521    shift. This can only be solved mathematically by a lower $\delta^{15}N^{av}$ value for the small

522    "anthropogenic" emissions in the early part of the firn record. A constant $\delta^{15}N^{av}$ source

523 signature would result in a small temporal change in $\delta^{15}N^{av}$ of atmospheric $N_2O$ in the

524 beginning of the record and increasing isotope trends with increasing emissions, similar to the

525 exponential curves that were fitted to the firn air data in Röckmann et al. (2003).

526 The $\delta^{18}O$ of the total source varies within (27.2±2.6) ‰ over the entire period. $\delta^{18}O$ does not

527 show significant decadal scale oscillations because the reconstructed scenario for $\delta^{18}O$ is even

528 more linear than the $\delta^{15}N^{av}$ scenario. For this reason, as explained above, in the best fit

529 scenario the $\delta^{18}O$ of the anthropogenic source for the initial 30 years has a more depleted

530 value starting with (7.7±2.6) ‰ in year 1940, reaching (31.1±2.6) ‰ in year 1975 and

531 remaining around this value until 2008 (Fig. 4). However, the relatively larger uncertainty

532 envelopes for the atmospheric history of $\delta^{18}O$ actually allow scenarios with smaller $\delta^{18}O$

533 changes in the beginning of the record and larger changes in the later period, which means

534 that the reconstruction does not exclude a constant value for the anthropogenic $\delta^{18}O$ source

535 signature. The available dataset thus does not allow quantifying a long-term trend in $\delta^{18}O$.

536 For the position dependent $^{15}N$ signatures of the total source no significant long-term trends

537 were detected. For $\delta^{15}N^{\alpha}$ no decadal scale variability is observed, whereas for $\delta^{15}N^{\beta}$ a

538 temporal variability is observed similar to the $\delta^{15}N^{av}$. The uncertainty ranges for $\delta^{15}N^{\alpha}$ and

539 $\delta^{15}N^{\beta}$ are about a factor 2 greater than for $\delta^{15}N^{av}$, which is due to the larger analytical error

540 that leads to higher uncertainties in the scenario reconstructions. $\delta^{15}N^{\alpha}$ varies in the range (–

541 3.0±1.9) ‰, $\delta^{15}N^{\beta}$ in the range (–11.7±2.3) ‰.

542 The temporal evolution of $\delta^{15}N^{\alpha}$ of the anthropogenic source looks similar to that of $\delta^{18}O$, but

543 with even larger variations and uncertainties with a total average of (–8.1±1.7) ‰. $\delta^{15}N^{\alpha}$

544 increased from (–18.2±1.7) ‰ in 1940 to an average of (-5.4±1.7) ‰ in 1975 and retained

545 this value until 2008. In contrast, $\delta^{15}N^{\beta}$ is similar to that of $\delta^{15}N^{av}$ with a total anthropogenic

546 source average of (–26.1±8.4). $\delta^{15}N^{\beta}$ initially decreases from (–19.1±8.4) ‰ to (-42.0±8.4) ‰

547 in 1955 only to increase again to (-10.6±8.4) ‰ in year 1990 and then decrease again to (-

548 26.0±8.4) ‰ in 2008.

## 4 Discussion

550 The $N_2O$ mole fraction atmospheric history from our multi-site reconstruction is in agreement

551 with recent work from Meinshausen et al. (2016) who combined all available published $N_2O$

552 data (atmospheric, firn, ice) in order to reconstruct a historical atmospheric record of the past

553    2000 years. It differs slightly from the one determined by Battle et al. (1996) and to smaller

554    extent with Machida et al. (1995).

555    Battle et al. (1996) collected firn air data and Machida et al. (1995) used ice data. Both studies

556    used samples from a single Antarctic site. One could argue that the difference is due to an

557    interhemispheric difference, but it is too large to be explained by this alone. In the past, $N_2O$

558    mole fraction measurements have been reported on different calibration scales, which is likely

559    to explain part of the differences between individual studies. Furthermore, differences in the

560    firn air model and possible differences between sites may contribute. In our case we used

561    measurements from 5 sites to constrain our model while Battle et al. (1996) and Machida et

562    al. (1995) used only one site. In addition, the atmospheric histories of up to 9 known gases

563    (depending on site, Witrant et al. 2012) were used to constrain diffusivity in our model while

564    Battle et al. (1996) only used two gases."

565    From the combination of the firn air reconstruction with a simple two-box model we conclude

566    that $N_2O$ emissions increased from (11.9±1.7) Tg $a^{-1}$ N in 1940 to (16.4±1.7) Tg $a^{-1}$ N in

567    2008. This agrees, within uncertainties, with previous firn reconstruction studies from

568    Ishijima et al. (2007) and Park et al. (2012) and bottom-up approaches using emission

569    databases (Syakila and Kroeze, 2013; Kroeze et al., 1999). A more recent study by Thompson

570    et al. (2014b) performed inversions of atmospheric measurements for 2006 to 2008 with

571    multiple models and reported emissions of 16.1-18.7 Tg $a^{-1}$ N for 2008, which is also in

572    agreement with our findings.

573    To investigate the effect the $N_2O$ lifetime on the $N_2O$ isotopic signatures (Prather et al. (2015)

574    we performed a sensitivity study where we linearly changed the $N_2O$ lifetime from 123 years

575    pre-industrially (≈1750) to 119 years in modern times (2008). The results are shown in

576    Appendix D, where the effect on the emission strength and isotopic composition is discussed

577    in detail. Results from this sensitivity study showed that the effect of a decreasing lifetime

578    gives higher $N_2O$ emissions for year 2008 while keeping the same pre-industrial value,

579    confirming the sensitivity to the lifetime in line with Prather et al. (2015). This change in

580    lifetime in the model leads to changes in the isotope signatures of the order of (2.0±1.0) ‰.

581    The lifetime effect is most pronounced for the earliest part of the record (<1970) where the

582    reconstruction uncertainties are larger than this systematic uncertainty.

583    We furthermore investigated the sensitivity to the value of $F_{exch}$ (stratosphere – troposphere

584    flux) between a low and high value of 0.16 and 0.28 Tmol $s^{-1}$, respectively following

585  Appenzeller et al. (1996) and Holton et al. (1990) with the default value being 0.22 Tmol s$^{-1}$.

586  As shown in Appendix D, the isotope values are not very sensitive to the changes in $F_{exch}$, the

587  results are well within the uncertainty envelopes.

588  The increase in $N_2O$ emissions over the past decades resulted in an overall decrease of all

589  isotopic signatures of atmospheric $N_2O$ with time. The isotopic signature of the total source of

590  $N_2O$ (Fig. 4, middle panels) is strongly depleted in all heavy isotopes compared to

591  tropospheric $N_2O$ (Table 3), which is due to the strong enrichment associated with the

592  removal in the stratosphere. In Table 3 the isotopic composition for the pre-industrial period

593  ($\approx$1750) ($\delta_{nat,pi}$) is compared with the derived anthropogenic source signature derived from

594  our multi-site reconstruction ($\delta_{anth}$, averaged from 1940 to 2008). The results show that the

595  anthropogenic source is more depleted in heavy isotopes than the natural one for all

596  signatures, confirming results from studies prior to firn air measurements (Rahn and Wahlen,

597  2000), and from studies that used forward firn air modelling on measurements from individual

598  sites (Park et al., 2012; Ishijima et al., 2007; Röckmann et al., 2003). It is important to

599  remember that we assume the natural sources to be constant, but the method itself does not

600  provide evidence for this.

601  Anthropogenic $N_2O$ emissions are dominated by agricultural soil (70 %) with smaller

602  contributions from automobiles, coal combustion, biomass burning and industry. Oceanic

603  emissions were previously assumed to be only natural. However, the latest IPCC Assessment

604  Report (Ciais et al., 2013) for the first time separated oceanic emissions into a natural and an

605  anthropogenic component, e.g. due to atmospheric N deposition to rivers (Syakila and

606  Kroeze, 2011; Duce et al., 2008; Kroeze et al., 2005). The oceanic fraction of the

607  anthropogenic source was estimated as 1 Tg a$^{-1}$ N.

608  $N_2O$ emitted from agricultural soils and biomass burning is more depleted in $\delta^{15}N^{av}$ and $\delta^{18}O$

609  than the tropospheric background (Park et al., 2011; Goldberg et al., 2010; Ostrom et al.,

610  2010; Tilsner et al., 2003; Perez et al., 2001; 2000) while $N_2O$ emitted from other minor

611  sources, such as automobiles, coal combustion and industry, has values closer to tropospheric

612  $N_2O$ values (Syakila and Kroeze, 2011; Toyoda et al., 2008; Ogawa and Yoshida, 2005a;

613  2005b). An increase of strongly depleted agricultural emissions in the first part of our

614  reconstruction, followed by a decreasing relative contribution from agriculture and increasing

615  contributions from more enriched sources like industry, automobiles and coal combustion,

616  could qualitatively explain the reconstructed changes of isotope signatures of both the total

source and the anthropogenic component. The global $N_2O$ budget study from Syakila and Kroeze (2011) indicates that agricultural emissions were 78 % of the total during the 1940-1980 period with little input from industry, vehicle exhaust and coal combustion. After 1980 the relative share of agricultural emissions dropped to 64 %, while the other sources increased, supporting our suggestion.

According to FAO statistics (http://www.fao.org/faostat/en/#data/GY/visualize), emissions from synthetic nitrogenous fertilizers increased between 1961 and 1985, then stayed relatively constant or even decreased until 2000, and increased again after 2000. The reasons of the decrease between 1985 and 2000 are a shift towards organic soil cultivation in combination with more efficient agricultural methods and fertilizer use. This variation in fertilizer use qualitatively matches with the temporal evolutions of our reconstructed source signatures, but the trends in the reconstructions are likely too large to be explained by this source change only.

Although the decadal variability for $\delta^{15}N^{av}$ and $\delta^{15}N^{\beta}$ appears statistically significant with respect to the choice of scenarios constructed within the error bars of the firn air reconstruction, additional systematic uncertainties in this reconstruction could potentially produce such trends artificially from small undulations on the scenarios, since the emissions are related to the derivative of the trend. As it is possible to draw straight lines within uncertainty envelopes of the scenarios, the decadal variability may not be robust. An increase of the regularization term by 10 confirms that the generated scenarios are straight lines well withing the uncertainty envelopes, thus the decadal variability could be a artifact of the model (see Appendix C).

Additional evidence for potential changes in the $N_2O$ source composition between the pre-industrial and present atmosphere may be derived from the position-dependent $^{15}N$ signatures, quantified by the $^{15}N$ site preference. Table 3 shows that the difference in the $\delta^{15}N^{av}$ signature between the pre-industrial and the anthropogenic source derived from our reconstruction is primarily due to a change at position $\delta^{15}N^{\beta}$, whereas $\delta^{15}N^{\alpha}$ remains relatively constant. This is reflected by a larger difference in $\delta^{15}N^{sp}$ between natural and anthropogenic emissions, which could indicate a temporal change in production processes.

Sutka et al. (2006) suggested that there may be two distinct classes of $N_2O$ sources with different $\delta^{15}N^{sp}$. $N_2O$ produced during nitrification and fungal denitrification had a high $\delta^{15}N^{sp}$ of $(33\pm5)$ ‰ and $N_2O$ from denitrification and nitrifier denitrification had a low $\delta^{15}N^{sp}$ of

649 (0±5) ‰. Park et al., (2012) used these two endmembers to calculate a change in the relative
650 fractions of these source classes over time based on their firn air data. Although this approach
651 is strongly simplified and several other sources and factors may contribute (Toyoda et al.,
652 2015), we use the results from our box model calculations (Table 3) in a similar way to
653 estimate the fraction of the two source categories according to the following simple mass
654 balance calculation:

655 $$F_{high} = \frac{\delta^{15}N^{sp}_{meas} - \delta^{15}N^{sp}_{low}}{\delta^{15}N^{sp}_{high} - \delta^{15}N^{sp}_{low}} \qquad (11)$$

656 This returns a fractional contribution of the $\delta^{15}N^{sp}_{high}$ component of (19±4) % to the total pre-
657 industrial emissions and (35±11) % to the total present source. The errors were derived by
658 propagating the errors of the $\delta^{15}N^{sp}$ endmembers and $\delta^{15}N^{sp}_{meas}$ within the ranges stated above.
659 We note that the errors associated with the precise isotopic composition of the endmembers
660 are correlated if the values of $\delta^{15}N^{sp}$ for the two endmembers remain relatively constant in
661 time. Therefore, the change in the relative fraction of the two categories is likely better
662 constrained than the absolute values.

663 Splitting the total present emission strength into a natural (pre-industrial, 11.0 Tg a$^{-1}$ N) and
664 anthropogenic (5.4 Tg a$^{-1}$ N) component, we derive a fraction of the $\delta^{15}N^{sp}_{high}$ component
665 (which includes nitrification) of (54±26) % for the "anthropogenic" emissions. This is another
666 piece of evidence for agricultural sources being the main contributor to the $N_2O$ increase,
667 because nitrification-dominated agricultural emissions can be associated with the $\delta^{15}N^{sp}_{high}$
668 component.

669 The temporal changes of the derived fraction of nitrification are in good qualitative agreement
670 with the results from Park et al. (2012), who reported a change of (13±5) % from 1750 to
671 (23±13) % today. However, the absolute numbers derived from our study are higher than the
672 results from Park et al. (2012). The difference is due to the fact that different apparent isotope
673 fractionations during stratospheric removal ($\varepsilon_{app}$) are used in the mass balance model (Table
674 3; eq. 7,8). In our study we used the averaged lowermost stratospheric apparent isotope
675 fractionations from Kaiser et al. (2006), which we consider more representative than the
676 numbers used by Park et al. (2012). Using different values for $\varepsilon_{app}$ causes a shift in the
677 isotopic source signatures from the mass balance model. The choice of this value thus adds a

678      systematic source of uncertainty to the absolute value of the $\delta^{15}N_{high}^{sp}$ fractions reported above

679      ($F_{high}$).

680      Nevertheless, this systematic uncertainty should not alter the overall *change* in $F_{high}$ from pre-

681      industrial to modern times and the results from our multi-site reconstruction of the isotopic

682      composition of $N_2O$ thus confirm the suggestion by Park et al. (2012) that the relative

683      importance of the high-SP component (presumably nitrification) has increased with increasing

684      mole fraction since pre-industrial times.

685 **5    Conclusions**

686      The temporal evolution of the total $N_2O$ emission fluxes and the source isotopic composition

687      have been estimated in a top-down approach using a multi-site reconstruction of $N_2O$ mole

688      fraction and isotopic composition from 6 firn air samplings at 5 different Arctic and Antarctic

689      locations in a two-box model. The results from a mass balance model constrain the source

690      strength and suggest a total increase in $N_2O$ emissions of (4.5±1.7) Tg $a^{-1}$ N between the 1940

691      and 2008 due to anthropogenic processes. This agrees with previous top-down estimates, but

692      deviates from bottom-up model estimates, which suggest higher $N_2O$ emission increases. A

693      significant source of the uncertainty in top-down estimates is a possible change in the $N_2O$

694      lifetime over the reconstruction period, which we have quantified following the recent results

695      from Prather et al. (2015).

696      The reconstruction of mole fraction and isotopic composition was used to investigate

697      temporal changes in the isotopic signature of $N_2O$ emissions over the study period. The

698      average total source for $\delta^{15}N^{av}$ and $\delta^{15}N^{\beta}$ shows no statistically significant long-term trend but

699      possibly significant decadal scale variability. For $\delta^{18}O$ and $\delta^{15}N^{\alpha}$ of the total $N_2O$ source, no

700      significant temporal changes can be detected with the present dataset because the

701      uncertainties are large, especially in the beginning of the reconstruction period.

702      When the total source is split into a constant natural and a varying anthropogenic component,

703      the reconstruction of the $\delta$ values of the anthropogenic source indicates a significant increase

704      of $\delta^{15}N^{av}$ from the early to the modern part of the record. This originates from the near-linear

705      isotope histories of the best guess scenario, which would imply that small emissions in the

706      early part had a similar absolute effect on the $\delta$ values as stronger emissions in the latter part.

707      A similar effect for $\delta^{18}O$ is likely, but not significant given the larger uncertainties for this

708      signature.

709 Nevertheless, the isotope signal in $\delta^{15}N^{av}$ may also be a signal for changing source
710 contributions over time. Bottom-up models suggest that $N_2O$ emitted from agricultural soils
711 was the dominant contributor to the anthropogenic $N_2O$ increase in the first decades. Smaller
712 contributions due to emissions from more enriched sources, like industry, automobiles and
713 coal combustion increased. This may have contributed to an isotope enrichment of the
714 emissions, which is not detectable within the error bars for the other isotope signatures.
715 However, one has to be cautious with a firm interpretation of these trends since the
716 reconstruction method itself may also induce decadal variability if the smoothness of the
717 scenario is incorrectly constrained.

718 Results from the mass balance model yield an increase in $^{15}N$ site preference between the pre-
719 industrial and modern total $N_2O$ source. When this trend is evaluated with a simplified two-
720 endmember mixing model, the results suggest an increase of nitrification sources relative to
721 denitrification-related sources over the industrial period.

**References**

Allin, S. J., Laube, J. C., Witrant, E., Kaiser, J., McKenna, E., Dennis, P., Mulvaney, R., Capron, E., Martinerie, P., Röckmann, T., Blunier, T., Schwander, J., Fraser, P. J., Langenfelrs, R. L., and Sturges, W. T.: Chlorine isotope composition in chlorofluorocarbons CFC-11, CFC-12 and CFC-113 in firn, stratospheric and tropospheric air, Atmos. Chem. Phys., 15, 6867-6877, doi:10.5194/acp-15-6867-2015, 2015.

Battle, M., Bender, M., Sowers, T., Tans, P. P., Butler, J. H., Elkins, J. W., Ellis, J. T., Conway, T., Zhang, N., Lang, P., and Clarke, A. D.: Atmospheric gas concentrations over the past century measured in air from firn at South Pole, Nature, 383, 231-235, 1996.

Bernard, S., Röckmann, T., Kaiser, J., Barnola, J.-M., Fischer, H., Blunier, T., and Chappellaz, J.: Constraints on $N_2O$ budget changes since pre-industrial time from new firn air and ice core isotope measurements, Atmos. Chem. Phys., 6, 493–503, doi:10.5194/acp-6-493-2006, 2006.

Buizert, C., Sowers, T., and Blunier, T.: Assessment of diffusive isotopic fractionation in polar firn, and application to ice core trace gas records, Earth Planet. Sci. Lett., 361, 110–119, 2013.

Butterbach-Bahl, K., and Dannenmann, M.: Denitrification and associated soil $N_2O$ emissions due to agricultural activities in a changing climate, Curr. Op. Environ. Sus., 3(5), 389–395, doi:10.1016/j.cosust.2011.08.004, 2011.

Ciais, P., Sabine, C., Bala, G., Bopp, L., Brovkin, V., Canadell, J., Chhabra, A., DeFries, R., Galloway, J., Heimann, M., Jones, C., Le Quéré, C., Myneni, R.B., Piao, S., and Thornton, P.: Carbon and other biogeochemical cycles. Climate Change 2013: The Physical Science Basis, Contribution of Working Group I to the Fifth Assessmetn Report of the Intergovernmental Panel on Climate Change, Cambridge University Press, Cambridge, United Kingdom and New York, NY, USA, 2013.

Crutzen, P. J., Mosier, A. R., Smith, K. A., and Winiwarter, W.: $N_2O$ release from agro-biofuel production negates global warming reduction by replacing fossil fuels, Atmos. Chem. Phys., 8, 389-395, doi:10.5194/acp-8-389-2008, 2008.

761    Crutzen, P.J.: The role of NO and NO$_2$ in the chemistry of the troposphere and stratosphere,

762    Annual review of earth and planetary sciences, 7, 443-472, 1979.

763    Davidson, E. A.: The contribution of manure and fertilizer nitrogen to atmospheric nitrous

764    oxide since 1860, Nat. Geosci., 2(9), 659–662, doi:10.1038/ngeo608, 2009.

765    Duce, R. A., LaRoche, J., Altieri, K., Arrigo, K .R., Baker, A. R., Capone, D. G., Cornell, S.,

766    Dentener, F., Galloway, J., and Ganeshram, R. S.: Impacts of atmospheric anthropogenic

767    nitrogen on the open ocean, Science, 320, 893-897, 2008.

768    Freing, A., Wallace, D. W. R., and Bange, H. W.: Global oceanic production of nitrous oxide,

769    Phil. Trans. R. Soc. Lond., Series B, 367(1593), 1245–55, doi:10.1098/rstb.2011.0360, 2012.

770    Hirsch, A., Michalak, A., Bruhwiler, L., Peters, W., Dlugokencky, E., and Tans, P.: Inverse

771    modelling estimates of the global nitrous oxide surface flux from 1998-2001, Gl. Biochem.

772    Cycl., 20, GB 1008, doi: 10.1029/2004GB002443, 2006.

773    Holton, J. R.: On the global exchange of mass between stratosphere and troposphere, J.

774    Atmos. Sci. , 47(3), 392-395, 1990.

775    Houghton, J. T., Meira Filho, L. G., Bruce, J., Lee, H., Callander, B. A, Haites, E., Harris, N.,

776    and Maskell, K.: Climate Change 1994: Radiative Forcing of Climate Change and an

777    Evaluation of the IPCC IS 92 Emission Scenarios, Cambridge University Press, Cambridge,

778    UK, 1994.

779    Ishijima, K., Sugawara, S., Kawamura, K., Hashida, G., Morimoto, S., Murayama, S., Aoki,

780    S.: Temporal variations of the atmospheric nitrous oxide concentration and its $\delta^{15}$N and $\delta^{18}$O

781    for the latter half of the 20th century reconstructed from firn air analyses, J. Geophys. Res.,

782    112(D3), doi:10.1029/2006JD007208, 2007.

783    Kaiser, J., Brenninkmeijer, C.A.M., Röckmann, T.: Intramolecular $^{15}$N and $^{18}$O fractionation

784    in the reaction of N$_2$O with O($^1$D) and its implications for the stratospheric N$_2$O isotopic

785    signature, J. Geophys. Res., 107 (4214), doi:10.1029/2001JD001506, 2002.

786     Kaiser, J., Röckmann T., and Brenninkmeijer, C.A.M.: Complete and accurate mass
787     spectrometric isotope analysis of tropospheric nitrous oxide, J. Geophys. Res., 108(D15), 1–
788     17, doi:10.1029/2003JD003613, 2003.

789     Kaiser, J., Engel, A., Borchers, R., and Röckmann, T.: Probing stratospheric transport and
790     chemistry with new balloon and aircraft observations of the meridional and vertical $N_2O$
791     isotope distribution, Atmos. Chem. Phys., 6, 3535-3556, doi:10.5194/acp-6-3535-2006, 2006.

792     Kaiser, J., and Röckmann T.: Correction of mass spectrometric isotope ratio measurements
793     for isobaric isotopologues of $O_2$ ,CO, $CO_2$, $N_2O$ and $SO_2$, Rap. Commun. Mass Spec., 3997–
794     4008, doi: 10.1002/rcm.3812, 2008.

795     Kim, K. R., and Craig, H.: Nitrogen-15 and Oxygen-18 Characteristics of Nitrous Oxide: A
796     global perspective, Science, 262, 1855-1857, 1993.

797     Kim, K. R., Craig, H.: Two-isotope characterization of $N_2O$ in the Pacific Ocean and
798     constraints on its origin in deep water, Nature, 347, 58-61, doi:10.1038/347058a0, 1990.

799     Kool, D. M., Wrage, N., Oenema, O., Harris, D., and Groenigen, J. W. Van.: The $^{18}O$
800     signature of biogenic nitrous oxide is determined by O exchange with water, Rap. Commun.
801     Mass Spec., 104–108, doi:10.1002/rcm.3859, 2009.

802     Kroeze, C., Mosier, A., and Bouwman, L.: Closing the global $N_2O$ budget: a retrospective
803     analysis 1500-1994, Glob. Biogeochem. Cycl., 13, 1-8, doi: 10.1029/1998GB900020, 1999.

804     Kroeze, C., Dumont, E., and Seitzinger, S. P.: New estimates of global emissions of $N_2O$ from
805     rivers and estuaries, Environ. Science, 2, 159-165, doi:10.1080/15693430500384671, 2005.

806     Löscher, C.R., Kock, A., Könneke, M., LaRoche, J., Bange, H. W., and Schmitz, R. A.:
807     Production of oceanic nitrous oxide by ammonia-oxidizing archaea, Biogeosciences, 9, 2419-
808     2429, doi:10.5194/bg-9-2419-2012, 2012.

809     MacFarling Meure, C., Etheridge, D., Trudinger, C., Steele, P., Langenfelds, R., van Ommen,
810     T., Smith, A., and Elkins, J.: Law Dome CO2, CH4 and N2O ice core records extended 2000
811     years BP, Geophys. Res. Letters, 33, 2000-2003, doi:10.1029/2006GL026152, 2006.

812    Machida, T., Nakazawa, T., Fujii, Y., Aoki, S., and Watanabe, O.: Increase in the atmospheric

813    nitrous oxide concentration during the last 250 years, Geophys. Res. Letters, 22, 2921-2924,

814    1995.

815    Maeda, K., Toyoda, S., Shimojima, R., Osada, T., Hanajima, D., Morioka, R., and Yoshida,

816    N.: Source of nitrous oxide emissions during the cow manure composting process as revealed

817    by isotopomer analysis of and amoA abundance in betaproteobacterial ammonia-oxidizing

818    bacteria, Appl. Environ. Microbiol., 76(5), 1555–62, doi:10.1128/AEM.01394-09, 2010.

819    Martinerie, P., Nourtier-Mazauric, E., Barnola, J.-M., Sturges, W. T., Worton, D. R., Atlas,

820    E., Brasseur, G. P.: Long-lived halocarbon trends and budgets from atmospheric chemistry

821    modelling constrained with measurements in polar firn, Atmos. Chem. Phys, 9, 3911-3934,

822    doi:10.5194/acp-9-3911-2009, 2009.

823    McElroy, M. B., and McConnell, J. C.: Nitrous oxide: A natural source of stratospheric NO,

824    Journal of Atmospheric Sciences, 28, 1095-1098, 1971.

825    McLinden, C. A., Prather, M. J., Johnson M. S.: Global modeling of the isotopic analogues of

826    $N_2O$: Stratospheric distributions, budgets and the $^{17}O$-$^{18}O$ mass-independent anomaly, J.

827    Geophys. Res., 108(D8), doi:10.1029/2002JD002560, 2003.

828    Meinshausen, M., Vogel, E., Nauels, A., Lorbacher, K., Meinshausen, N., Etheridge, D.,

829    Frazer, P., Montzka, S. A., Rayner, P., Trudinger, C., Krummel, P., Beyerle, U., Cannadell, J.

830    G., Daniel., J. S., Enting, I., Law, R. M., O'Doherty, S., Prinn, R. G., Reimann, S., Rubino,

831    M., Velders, G. J. M., Vollmer, M. K., and Weiss, R.: Historical greenhouse gas

832    concentrations, Geosci. Model Dev. Discuss, doi:10.5194/gmd-2016-169, in review, 2016.

833    Minschwaner, K., Salawitch, R.J., McElroy, M.B.: Absorption of Solar Radiation by $O_2$:

834    Implications for $O_3$ and lifetimes of $N_2O$, $CFCl_3$, and $CF_2Cl_2$, J. Geophys. Res., 98, 10543-

835    10561, doi: 10.1029/93JD00223, 1993.

836    Ogawa, M., and Yoshida, N.: Intramolecular distribution of stable nitrogen and oxygen

837    isotopes of nitrous oxide emitted during coal combustion, Chemosphere, 61, 877-887, 2005a.

838    Ogawa, M., and Yoshida, N.: Nitrous oxide emission from the burning of agricultural residue.

839    Atmos. Environ., 39, 3421-3429, 2005b.

840 Ostrom, N. E., and Ostrom, P. H.: The isotopomers of Nitrous Oxide: Analytical

841 considerations and application to resolution of microbial production pathways, Baskaran, M.,

842 Handbook of Environmental Isotope Geochemisttry, Advances in Isotope Geochemistry,

843 Springer, Verlag, Berlin, Heidelberg, 453-476, 2011.

844 Park, S., Atlas, E. L., and Boering, K. A.: Measurements of $N_2O$ isotopologues in the

845 stratosphere: Influence of transport on the apparent enrichment factors and the isotopologue

846 fluxed to the troposphere, J. Geophys. Res., 109, doi:10.1029/2003JD003731, 2004.

847 Park, S., Croteau, P., Boering, K. A., Etheridge, D. M., Ferretti, D., Fraser, P. J., and

848 Trudinger, C. M.: Trends and seasonal cycles in the isotopic composition of nitrous oxide

849 since 1940, Nat. Geosci., *5*(4), 261–265, doi:10.1038/ngeo1421, 2012.

850 Pérez, T., Trumbonre, S. E, Tyler, S. C., Davidson, E. A., Keller, M., and Camargo, P. de.:

851 Isotopic variability of $N_2O$ emissions from tropical forest soils, Glob, Biogeochem. Cycl.,

852 14(2), 525-535, 2000.

853 Pérez, T., Trumbore, S. E., Tyler, S. C., Matson, P. A, Ortiz-Monasterio, I., Rahn, T., and

854 Griffith, D. W. T.: Identifying the agricultural imprint on the global $N_2O$ budget using stable

855 isotopes, J. Geophys. Res.,106(D9), 9869-9878, 2001.

856 Popp, B. N., Westley, M. B., Toyoda, S., Miwa, T., Dore, J. E, Yoshida, N., Rust, T. M.,

857 Sansone, F. J, Russ, M. E, Ostrom, N. E., and Ostrom, P. H: Nitrogen and oxygen

858 isotopomeric constraints on the origins and sea-to-air flux of $N_2O$ in the oligotrophic

859 subtropical North Pacific gyre, Glob, Biogeochem. Cycl., 16, 1064,

860 doi:10.1029/2001GB001806, 2002.

861 Potter, K. E.: Nitrous oxide ($N_2O$) isotopic composition in the troposphere: instrumentation,

862 observations at Mace Head, Ireland, and regional modeling, PhD thesis, Department of Earth,

863 Atmospheric, and Planetary Sciences at the Massachusetts Institute of Technology, 2011.

864 Prather, M. J., et al.: Measuring and modeling the lifetime of nitrous oxide including its

865 variability, J. Geophys. Res. Atmos., 120, 5693-5705, doi: 10.1002/2015JD023267, 2015.

866 Rahn, T., and Wahlen, M.: Stable isotope enrichment in stratospheric nitrous oxide, Science,

867 278, 1776-1778, doi: 10.1126/science.278.5344.1776, 1997.

868    Rahn, T., Zhang, H., Wahlen, M., and Blake, G. A.: Stable isotope fractionation during

869    ultraviolet photolysis of $N_2O$, Geophys. Res. Lett., 25, 4489-4492, 1998.

870    Rahn, T., and Wahlen, M.: A reassessment of the global isotopic budget of atmospheric

871    nitrous oxide, Glob. Biogeochem. Cycl., 14, 537-543, 2000.

872    Ravishankara, A. R., Daniel, J. S., and Portmann, R. W.: Nitrous oxide ($N_2O$): the dominant

873    ozone-depleting substance emitted in the 21st century, Science, 326(5949), 123–125,

874    doi:10.1126/science.1176985, 2009.

875    Röckmann, T., Kaiser, J., Brenninkmeijer, C. A. M., Crowley, J. N., Borchers, R., Brand, W.

876    A., and Crutzen, J.: Isotopic enrichment of nitrous oxide ($^{15}N^{14}NO$, $^{14}N^{15}NO$, $^{14}N^{14}N^{18}O$) in

877    the stratosphere and in the laboratory, J. Geophys. Res., 106(D10), 10403-10410,

878    doi:10.1029/2000JD900822, 2001.

879    Röckmann, T., Kaiser, J., Brenninkmeijer, C. A. M., and Brand, W. A.: Gas

880    chromatography/isotope-ratio mass spectrometry method for high-precision position-

881    dependent $^{15}N$ and $^{18}O$ measurements of atmospheric nitrous oxide, Rap. Commun. Mass

882    Spectrom. , 17(16), 1897–1908, doi:10.1002/rcm.1132, 2003.

883    Röckmann, T., Kaiser, J., Brenninkmeijer, C. A. M.: The isotopic fingerprint of the pre-

884    industrial and the anthropogenic $N_2O$ source, Atmos. Chem. Phys., 3, 315-323,

885    doi:10.5194/acp-3-315-2003, 2003.

886    Röckmann, T., and Levin, I.: High-precision determination of the changing isotopic

887    composition of atmospheric $N_2O$ from 1990 to 2002, J. Geophys. Res., 110(D21), 1–8,

888    doi:10.1029/2005JD006066, 2005.

889    Santoro, A. E., Buchwald, C., Mcllvin, M. R., and Casciotti, K. L.: Isotopic signature of $N_2O$

890    produced by marine ammonia-oxidizing archaea,Science, 333(6047), 1282–1285,

891    doi:10.1126/science.1208239, 2011.

892    Sapart, C. J., van der Veen, C., Vigano, I., Brass, M., van de Wal, R. S. W., Bock, M.,

893    Fischer, H., Sowers, T., Buizert, C., Sperlich, P., Blunier, T., Behrens, M., Schmitt, J., Seth,

894    B., and Röckmann, T.: Simultaneous stable isotope analysis of methane and nitrous oxide of

895    ice core samples, Atmos. Meas. Tech., 4, 2607–2618, doi:10.5194/amt-4-2607-2011, 2011.

896  Sapart, C. J., Martinerie, P., Witrant, E., Chappellaz, J., van de Wal, R. S. W., Sperlich, P.,

897  van der Veen, C., Bernard, S., Sturges, W. T., Blunier, T., Schwander, J., Etheridge, D.,

898  Röckmann, T.: Can the carbon isotopic composition of methane be reconstructed from multi-

899  site firn air measurements?, Atmos. Chem. Phys., 13, 6993-7005, doi:10.5194/acp-13-6993-

900  2013, 2013.

901  Stocker, T. F., Qin, D., Plattner, G.-K., Tingor, M., Allen, S. K., Boschung, J., Nauels, A.,

902  Xia, Y., Bex, V., Midgley, P. M. et al.: IPCC, 2013: Climate Change 2013: The physical

903  Science Basis. Contribution of Working Group I to the Fifth Assessment Report of the

904  Intergovernmental Panel on Climate Change, Cambridge University Press, Cambridge, United

905  Kingdom and New York, NY, USA, 2013.

906  Sowers, T., Rodebaugh, A., Yoshida, N., and Toyoda, S.: Extending records of the isotopic

907  composition of atmospheric $N_2O$ back to 1800 A.D. from air trapped in snow at the South

908  Pole and the Greenland Ice Sheet Project II ice core, Global Biogeochemical Cycles, 16(4),

909  1–10, doi: 10.1029/2002GB001911, 2002.

910  SPARC, 2013: SPARC Report on the Lifetimes of Stratospheric Ozone-Depleting

911  Substances, Their Replacements, and Related Species, edited by: Ko, M., Newman, P.,

912  Reimann, S., and Strahan, S, SPARC Report No. 6, WCRP-15, Zurich, Switzerland, 2013.

913  Suntharalingam, P., Buitenhuis, E., Le Quéré, C., Dentener, F., Nevison, C., Butler, J. H., and

914  Forster, G.: Quantifying the impact of anthropogenic nitrogen deposition on oceanic nitrous

915  oxide, Geophysical Research Letters, 39, doi:10.1029/2011GL050778, 2012.

916  Sutka, R. L., Ostrom, N. E., Ostrom, P. H., Breznak, J. A., Gandhi, H., Pitt, A. J., and Li, F.:

917  Distinguishing Nitrous Oxide Production from Nitrification and Denitrification on the Basis

918  of Isotopomer Abundances, Appl. Environ. Microbiol., 72(1), 638–644,

919  doi:10.1128/AEM.72.1.638-644.2006, 2006.

920  Syakila, A., Kroeze, C., and Slomp, C. P.: Neglecting sinks for $N_2O$ at the earth's surface:

921  does it matter?, Journal of Integrative Environmental Sciences, 7, 79-87,

922  doi:10.1080/1943815X.2010.497492, 2010.

923  Syakila, A., and Kroeze, C.: The global nitrous oxide budget revisited, Greenhouse Gas

924  Measurement and Management, 1(1), 17–26, doi:10.3763/ghgmm.2010.0007, 2011.

925    Thompson, R. L., Ishijima, K., Saikawa, E., Corazza, M., Karstens, U., Patra, P. K.,
926    Bousquet, P. (2014). TransCom N$_2$O model inter-comparison, Part II: Atmospheric inversion
927    estimates of N$_2$O emissions. *Atmospheric Chemistry and Physics Discussions*, *14*(4), 5271–
928    5321.

929    Thompson, R. L., Patra, P. K., Ishijima, K., Saikawa, E., Corazza, M., Karstens, U.,
930    Bousquet, P.: TransCom N$_2$O model inter-comparison – Part 1: Assessing the influence of
931    transport and surface fluxes on tropospheric N$_2$O variability, Atmos. Chem. Phys. 14, 4349-
932    4368, doi:10.5194/acp-14-4349-2014, 2014.

933    Toyoda, S., Yamamoto, S., Arai, S., Nara, H., Yoshida, N., Kashiwajura, K., and Akiyama,
934    K.: Isotopomeric characterization of N$_2$O produced, consumed and, emitted by automobiles.,
935    Rap. Comm. in Mass Spec., 22, 603-612, doi:10.1002/rcm.3400, 2008.

936    Wang, Z., Chappellaz, J., Martinerie, P., Park, K., Petrenko, V., Witrant, E., Emmons, L. K.,
937    Blunier, T., Brenninkmeijer, C. A. M., and Mak, J. E.: The isotopic record of Northern
938    Hemisphere atmospheric carbon monoxide since 1950: implications for the CO budget,
939    Atmos. Chem. Phys., 12, 4365-4377, doi:10.5194/acp-12-4365-2012, 2012.

940    Westley, M. B., Popp, B. N., and Rust, T. M.: The calibration of the intramolecular isotope
941    distribution in nitrous oxide measured by isotope ratio mass spectrometry, Rap. Comm. in
942    Mass. Spec., 21(3), 391-405, doi:10.1002/rcm.2828, 2007.

943    Witrant, E., Martinerie, P., Hogan, C., Laube, J.C, Kawamura, K., Capron, E., Montzka, S.
944    A., Dlugokencky, E. J., Etheridge, D., Blunier, T., and Sturges, W. T.: A new multi-gas
945    constrained model of trace gas non-homogeneous transport in firn: evaluation and behavior at
946    eleven polar sites, Atmos. Chem. Phys., 12, 11465-11483, doi:10.5194/acp-12-11465-2012,
947    2012.

948    Witrant, E., Martinerie, P.: Input estimation from sparse measurements in LPV systems and
949    isotopic ratios in polar firn, IFAC Joint conferenc SSSC - 5th Symposium on System
950    Structure and Control, Grenoble, France, 150, 2013.

951    Yoshida, N., and Toyoda, S.: Constraining the atmospheric N$_2$O budget from intramolecular
952    site preference in N$_2$O isotopomers, Nature, 405, 330–334, doi:10.1038/35012558, 2000.

953

954 Table 1. Site information on the drilling locations of the North Greenland Ice core Project

955 (NGRIP-01[Ishijima], NGRIP-01[Bernard]), Berkner Island (BKN-03), North Greenland Eemian Ice

956 drilling Project (NEEM-EU-08, NEEM-09), Dome Concordia (DC-99) and Dronning Maud

957 Land (DML-98), where firn air samples were collected, and two key meteorological variables

958 of each site.

| Site | Location | Mean annual temperature ($^o$C) | Surface accumulation rate (water equivalent) (cm a$^{-1}$) | Sampling year |
|---|---|---|---|---|
| NGRIP-01[1] | 75$^o$ N 42$^o$ W | -31 | 20 | 2001 |
| BKN-03[2] | 79$^o$ S 45$^o$ W | -26 | 13 | 2003 |
| NEEM-EU-08 | 77.4$^o$ N 51.1$^o$ W | -29 | 22 | 2008 |
| NEEM-09 | 77.4$^o$ N 51.1$^o$ W | -29 | 22 | 2009 |
| DC-99[3] | 75$^o$ S 123$^o$ E | -53 | 3 | 1999 |
| DML-98[3] | 75$^o$ S 65$^o$ E | -38 | 6 | 1998 |

959 [1] Data retrieved from Bernard et al. (2006), Ishijima et al. (2007)

960 [2] Data retrieved from Bernard et al. (2006)

961 [3] Data retrieved from Röckmann et al. (2003)

962

963

964

965

966

967

968

969

970

971

972    Table 2. Detailed information in the mole fraction and the isotopic composition of the

973    laboratory reference gases used for correcting each set of firn air samples.

| Site | Sampling year | Mole fraction (nmol mol$^{-1}$) | $\delta^{15}N^{av}$ (‰) | $\delta^{18}O$ (‰) | $\delta^{15}N^{\beta}$ (‰) | $\delta^{15}N^{\alpha}$ (‰) |
|------|---------------|---------------------------------|-------------------------|--------------------|----------------------------|-----------------------------|
| NGRIP-01 | 2001 | 318 | 6.64 | 44.61 | -2.79 | 16.07 |
| BKN-03 | 2003 | 318 | 6.64 | 44.61 | -2.79 | 16.07 |
| NEEM-EU-08 | 2008 | 324 | 6.22 | 44.40 | -3.08 | 15.52 |
| NEEM-09 | 2009 | 318 | 6.38 | 44.92 | -2.66 | 15.41 |
| DC-99 | 1999 | 318 | 6.64 | 44.61 | -2.79 | 16.07 |
| DML-98 | 1998 | 318 | 6.64 | 44.61 | -2.79 | 16.07 |

974

975

976

977

978

979

980

981

982

983

984

985

986

987

988

989

Table 3. Emission fluxes and isotopic composition of the natural and anthropogenic source

results from the mass balance model. Stratospheric isotope fractionation ($\varepsilon_L$) used in the mass

balance model, and the respective results from Park et al. (2012).

**Natural source ($E_{nat}$, $\delta_{nat,pi}$)[1]**

| | This study | Park et al. (2012) |
|---|---|---|
| $E_{nat}$ (Tg a$^{-1}$ N) | 11.0±1.7 | 11.1 |
| $\delta^{15}N^{av}$ (‰) | -5.2±0.2 | -5.3±0.2 |
| $\delta^{18}O$ (‰) | 33.1±0.2 | 32.0±0.2 |
| $\delta^{15}N^{\alpha}$ (‰) | -1.9±1.0 | -3.3±1.0 |
| $\delta^{15}N^{\beta}$ (‰) | -8.3±1.1 | -7.5±1.1 |
| $\delta^{15}N^{sp}$ (‰) | 6.4±1.5 | 4.2±1.5 |

**Anthropogenic source ($E_{anth}$, $\delta_{anth}$)**

| | This study | Park et al. (2012) |
|---|---|---|
| $E_{anth}$ (Tg a$^{-1}$ N) | 5.4±1.7 | 6.6 |
| $\delta^{15}N^{av}$ (‰) | -18.2±2.6 | -15.6±1.2 |
| $\delta^{18}O$ (‰) | 27.2±2.6 | 32.0±1.3 |
| $\delta^{15}N^{\alpha}$ (‰) | -8.1±1.7 | -7.6±6.2 |
| $\delta^{15}N^{\beta}$ (‰) | -26.1±8.4 | -20.5±7.1 |
| $\delta^{15}N^{sp}$ (‰) | 18.0±8.6 | 13.1±9.4 |

**Stratospheric Loss[1]**

| | This study | Park et al. (2012) |
|---|---|---|
| $F_{exch}$ (Tmol s$^{-1}$) | 0.22 | NA |
| L (Tg a$^{-1}$ N) | 12.3 | NA |
| $\varepsilon_{app}$ $^{15}N^{av}$ (‰) | -16.2 | -14.9 |
| $\varepsilon_{app}$ $^{18}O$ (‰) | -13.4 | -13.3 |
| $\varepsilon_{app}$ $^{15}N^{\alpha}$ (‰) | -23.0 | -22.4 |
| $\varepsilon_{app}$ $^{15}N^{\beta}$ (‰) | -9.4 | -7.1 |

| N₂O Lifetime (a) | | |
|---|---|---|
| | **This study** | **Park et al. (2012)** |
| | 123 | 120 |

993 [1]$\delta_{atm,pi}$ values are from Park et al. (2012) who also calculated $\delta_{nat,pi}$ and $\delta_{anth}$ in a two-box model. The values are (9.3±0.2) (

994 ‰) for $\delta^{15}N^{av}$, (45.5±0.2) ( ‰) for $\delta^{18}O$, (18.8±1.0) ( ‰) and (-0.6±1.1) ( ‰) for $\delta^{15}N^{\alpha}$ and $\delta^{15}N^{\beta}$ respectively. In this study,

995 the $\delta_{anth}$ values are the averaged values over the whole investigated period. $\varepsilon_L$ values used in this study are averaged values

996 from the lower stratosphere from Kaiser et al. (2006) and $\varepsilon_L$ values from Park et al. (2012) were used from Park et al. (2004).



997
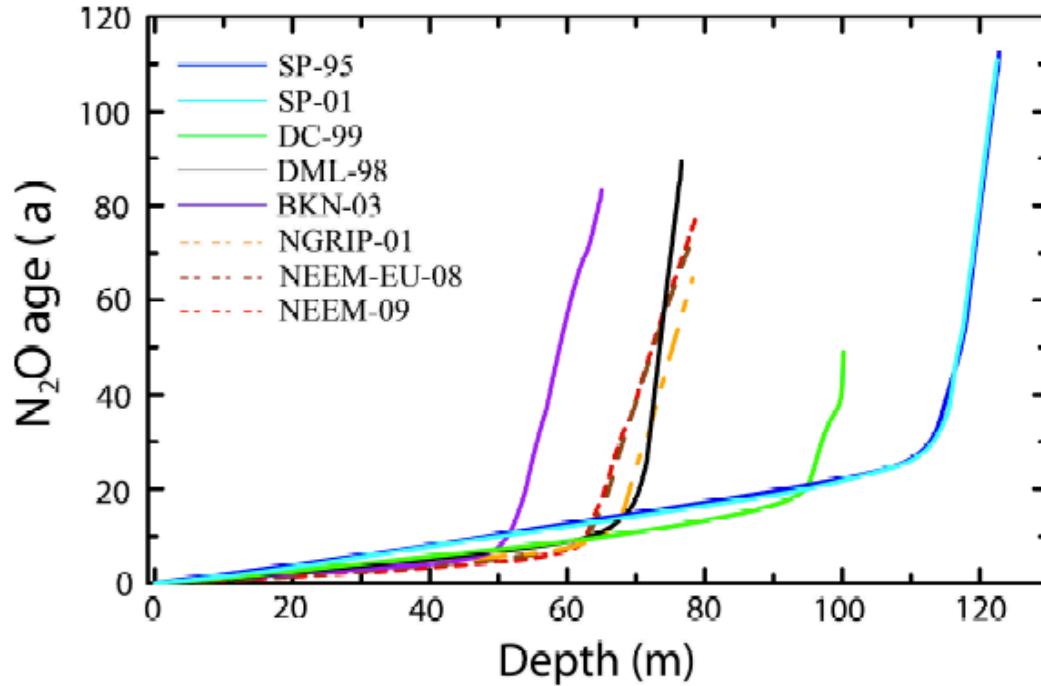
998 Figure 1. N₂O mean ages in firn versus depth. The dashed lines represent the sites from the

999 NH (North Greenland Ice-core Project [NGRIP-01 Bernard], North Eemian Ice-core Project

1000 [NEEM-09, NEEM-EU-08]) and the solid lines the SH sites (South Pole [SP-01, SP-95],

1001 Dome C [DC-99], Dronning Maud Land [DML-98] and Berkner Island [BKN-03]). The

1002 numbers accompanying the sites are the corresponding drilling years. Marker X indicates the

1003 transition between the firn diffusive zone and the bubble close-off zone for each site. Dashed

1004 orange line NGRIP-01, dashed brown NEEM-EU-08, dashed red NEEM-09, purple line

1005 BKN-03, black DML-98, green DC-99, blue SP-95 and light blue SP-01.
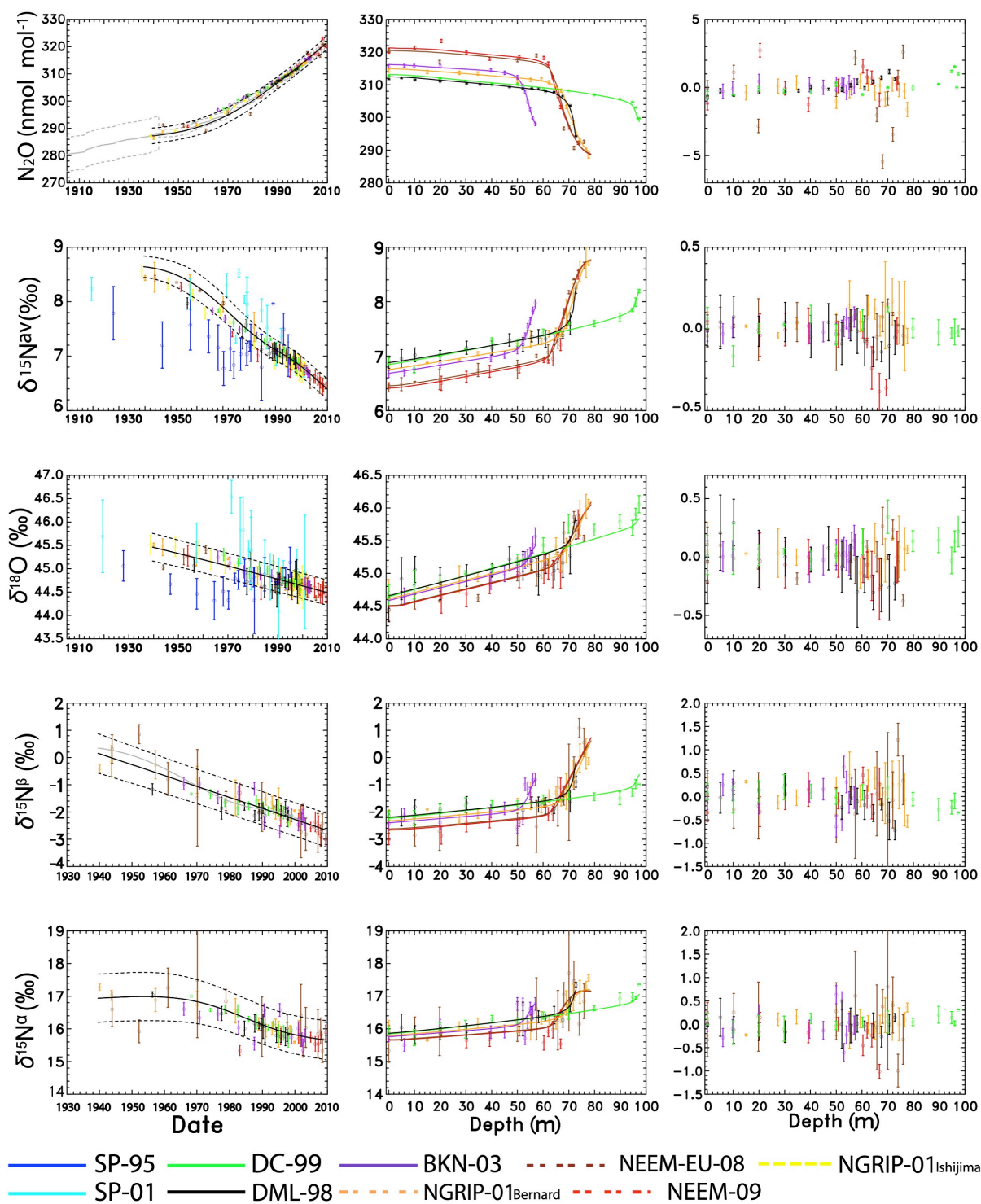
Figure 2. Left: Reconstructed atmospheric scenarios (black solid line with dashed lines indicating the 2 σ uncertainty intervals) and results of the firn air samples (corrected for firn fractionation) plotted at their respective assigned mean age. Middle: corresponding depth profiles, symbols show the measurements and solid lines the results of the forward model using the best estimate scenario as input. Right: model data discrepancies as a function of depth. Orange: NGRIP-01$_{Bernard}$, Yellow: NGRIP-01$_{Ishijima}$, Brown: NEEM-EU-08, Red NEEM-09, Purple: BKN-03, Black: DML-98, Green: DC-99, Blue: SP-95 and Light Blue: SP-01. Data from NGRIP-01$_{Ishijima}$ SP-95 and SP-01 were not used in the atmospheric reconstruction and are only plotted for comparison purposes here.
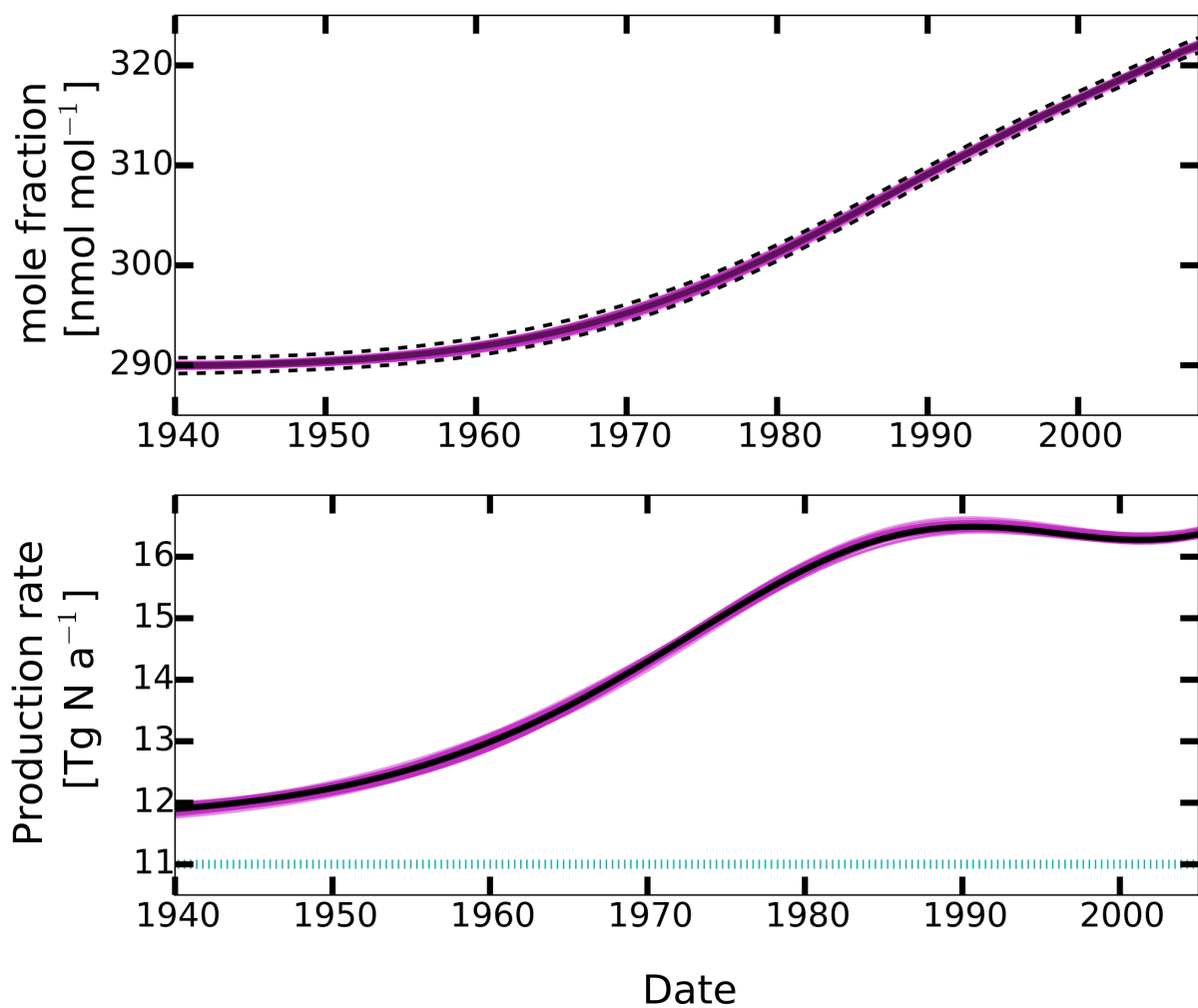
Figure 3: Top panel. $N_2O$ mole fraction history constrained with the most precise data at NEEM only to narrow the uncertainties (solid black line with uncertainty envelopes as dashed black lines) and the scenarios within the uncertainty envelopes that were used in the mass balance model (magenta lines) to evaluate the uncertainties of the atmospheric modelling results.

Bottom panel. $N_2O$ production rate as calculated from the mass balance model. The solid black line represents the result for the best fit reconstruction while magenta lines represent the results for the individual scenarios from the top panel. Dotted light green line denotes the natural source emissions which were kept constant in our model runs.
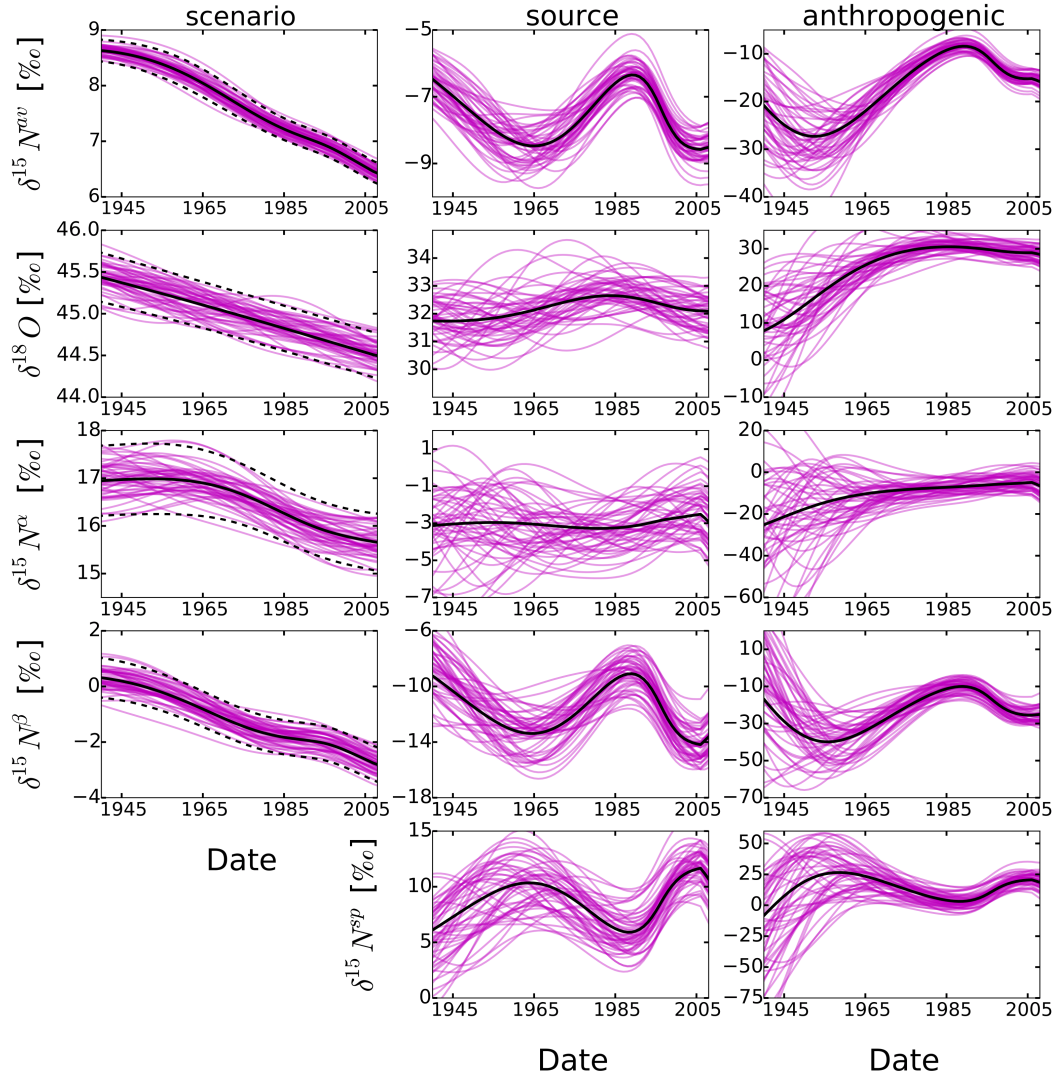
Figure 4: Left panels: Historic evolution of $\delta^{15}N^{av}$, $\delta^{18}O$, $\delta^{15}N^{\alpha}$ and $\delta^{15}N^{\beta}$ in $N_2O$ as derived from the firn air reconstruction. Middle panels: isotope signatures of the total emitted $N_2O$. Right panels: isotope signatures of the anthropogenic source, respectively. The solid black line represents the best-fit scenario while the dashed ones represent the respective uncertainties as determined by the reconstruction method. Magenta lines represent the emissions that are required to produce the magenta $N_2O$ histories in the left panels.

**Appendix A: Effect of firn fractionation on isotopic composition**
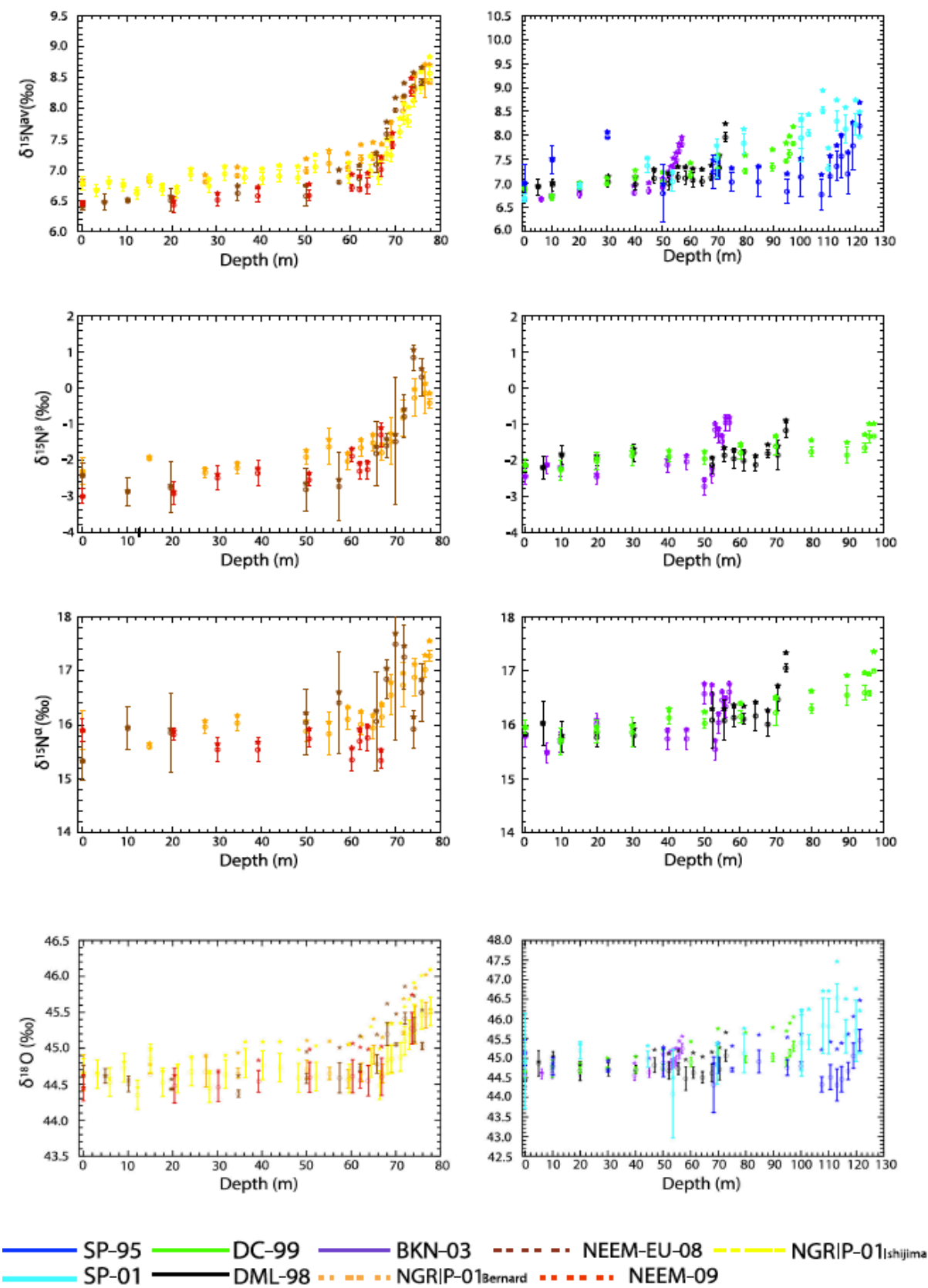
1048 Figure A1: Effect of firn fractionation on $N_2O$ isotopic composition in firn. Original

1049 measurements are plotted as stars, data corrected for firn fractionation are plotted as circles

1050 with error bars. The left hand side shows Northern hemisphere sites, orange: NGRIP-01$_{Bernard}$,

1051 yellow: NGRIP-01$_{Ishijima}$, brown: NEEM-EU-08, red NEEM-09 and the right hand side shows

1052 Southern hemisphere sites, purple: BKN-03, black DML-98, green DC-99, blue SP-95 and

1053 light blue SP-01

1054 **Appendix B: Data processing**

1055 In this study isotope deltas ($\delta$) are used to denote the relative $^{15}N/^{14}N$ and $^{18}O/^{16}O$ ratio

1056 difference of $N_2O$ in firn air with respect to a standard reference,

1057 $$\delta^{15}N = \frac{R_{sample}}{R_{standard}} - 1 \qquad (1)$$

1058 where R represents the $^{15}N/^{14}N$ or $^{18}O/^{16}O$ abundance ratio of a standard or a sample. $\delta^{15}N$

1059 values are reported relative to $^{15}R$ of atmospheric $N_2$, $\delta^{18}O$ values relative to $^{18}R$ of Vienna

1060 Mean Standard Ocean Water (VSMOW). The $^{15}N/^{14}N$, $^{18}O/^{16}O$ and position dependent

1061 $^{15}N/^{14}N$ isotope ratios were derived from measurement of the $m/z$ 45 / $m/z$ 44, $m/z$ 46 / $m/z$ 44

1062 and $m/z$ 31 / $m/z$ 30 ion current ratios according to Kaiser et al., (2008), assuming a constant

1063 $^{17}O$ excess of 0.9 ‰.

1064 There is a disagreement between reported trends of the position dependent $\delta^{15}N^{av}$ values

1065 reported in the literature from firn air on the one hand and archived air samples on the other

1066 hand (Park et al., 2012; Ishijima et al., 2007; Bernard et al., 2006; Röckmann and Levin,

1067 2005; Röckmann et al., 2003; Sowers et al., 2002). In principle the temporal trend measured

1068 directly on archived air samples should be fully consistent with top firn air samples of the

1069 various data sets, which were collected over a decade or more, since the air in the diffusive

1070 zone is not very old. However, this is not the case. Using the high-precision determination of

1071 the temporal trend of the $N_2O$ isotope signatures on archived air samples from Röckmann and

1072 Levin (2005) as reported in section 2.4 we rescale the different firn profiles to match this

1073 trend in the diffusive zone by interpolating the measurements from the diffusive zone of all

1074 sites to DC-99 ($\delta_{INT}$). By using the firn model – assigned mean age of each sample, The

1075 maximum age difference from diffusive zone to surface corresponds to $\Delta age = \Delta_{DC\,t-t_0} = 10$ a.

1076 Below you can find the equations used:

1077 $$\delta_{INT} = \delta_{t-t_0} - \delta_{DC\,t-t_0} + m\,(\Delta_{t-t_0} - \Delta_{DC\,t-t_0}) \qquad (2)$$

1078     $\delta_{Final} = \delta_{meas} - (\delta_{exp} - \delta_{INT})$              *(3)*

1079     Where $m$ is the slope connecting the two points we want to interpolate. The applied scaling

1080     ($\delta_{Final}$) is given in the Table B1 below. To bring the data to the most recent international scale,

1081     NOAA-2006A, we used an equation extracted from a correlation between a scale ratio of

1082     NOAA-2006A to CSIRO versus the mole fraction of $N_2O$. The correlation showed higher

1083     scale ratio for low fraction values and lower scale ratio for higher mole fraction values. The

1084     equation extracted is given below:

1085     $y(NOAA\text{-}2006) = -1.535 \times 10^{-4}\, y^2(CSIRO) + 1.045\, y(CSIRO)$        *(4)*

Table B1. Implemented scaling for $N_2O$ mole fraction and isotopic composition. The re-scaled average was extracted from the diffusivity zone for each site, which corresponds to the top 50 m. The expected trends are averaged values from CSIRO (http://www.csiro.au/greenhouse-gases) for the last 30 years for the mole fraction and measured trends from Röckmann and Levin (2005) for the isotopic composition. The rather large corrections to the isotope data from the SP-01 and SP-95 drillings are likely due to inter-laboratory scale differences.

| Site | $y(N_2O)(nmol\ mol^{-1})$ | | |
| | Re-scaled average | Expected trend change | Correction |
| --- | --- | --- | --- |
| DML-98 | 0.09±0.29 | -0.80±0.06 | -0.89±0.32 |
| NGRIP-01$_{Bernard}$ | 3.39±0.54 | 1.60±0.06 | -1.79±0.54 |
| NGRIP-01$_{Ishijima}$ | 4.12±0.32 | 1.60±0.06 | -2.52±0.32 |
| BKN-03 | 3.47±0.22 | 3.20±0.06 | -0.27±0.23 |
| NEEM-EU-08 | 3.57±1.81 | 7.20±0.06 | 3.63±1.81 |
| NEEM-09 | 8.84±1.82 | 8.00±0.06 | -0.84±1.82 |

| Site | $\delta^{15}N^{av}$ (‰) | | |
| | Re-scale average | Expected trend change | Correction |
| --- | --- | --- | --- |
| SP-95 | 1.43±0.56 | 0.16±0.00 | -1.27±0.56 |
| DML-98 | -0.18±0.12 | 0.04±0.00 | 0.22±0.12 |
| SP-01 | 0.22±0.22 | -0.08±0.00 | -0.30±0.22 |
| NGRIP -01$_{Bernard}$ | -0.18±0.07 | -0.08±0.00 | 0.10±0.07 |
| NGRIP -01$_{Ishijima}$ | 0.17±0.13 | -0.08±0.00 | -0.25±0.13 |
| BKN-03 | -0.17±0.12 | -0.16±0.00 | 0.01±0.12 |
| NEEM-EU-08 | -0.63±0.15 | -0.36±0.00 | 0.27±0.15 |
| NEEM-09 | -0.43±0.05 | -0.40±0.00 | -0.03±0.05 |

| Site | $\delta^{18}O$ (‰) | | |
| --- | --- | --- | --- |
| | Re-scale average | Expected trend change | Correction |
| SP-95 | -0.88±0.27 | 0.08±0.00 | 0.96±0.27 |
| DML-98 | 0.26±0.15 | 0.02±0.00 | -0.24±0.15 |
| SP -01 | 0.74±0.62 | -0.04±0.00 | -0.78±0.62 |
| NGRIP-01$_{Bernard}$ | -0.08±0.05 | -0.04±0.00 | 0.04±0.05 |
| NGRIP-01$_{Ishijima}$ | -0.17±0.12 | -0.04±0.00 | 0.13±0.12 |
| BKN-03 | 0.02±0.06 | -0.08±0.00 | -0.10±0.06 |
| NEEM-EU-08 | -0.21±0.15 | -0.19±0.00 | 0.02±0.15 |
| NEEM-09 | 0.28±0.04 | -0.21±0.00 | -0.49±0.04 |

| Site | $\delta^{15}N^{\beta}$ (‰) | | |
| --- | --- | --- | --- |
| | Re-scale average | Expected trend change | Correction |
| DML-98 | -0.41±0.20 | 0.06±0.02 | 0.47±0.20 |
| NGRIP-01$_{Bernard}$ | -0.10±0.25 | -0.13±0.02 | -0.02±0.25 |
| BKN-03 | -0.53±0.30 | -0.26±0.02 | 0.27±0.30 |
| NEEM-EU-08 | -0.33±0.27 | -0.58±0.02 | -0.25±0.27 |
| NEEM-09 | -0.14±0.17 | -0.64±0.02 | -0.50±0.17 |

| Site | $\delta^{15}N^{\alpha}$ (‰) | | |
| --- | --- | --- | --- |
| | Re-scale average | Expected trend change | Correction |
| DML-98 | 0.09±0.11 | 0.01±0.02 | -0.08±0.11 |
| NGRIP-01$_{Bernard}$ | -0.26±0.19 | -0.03±0.02 | 0.23±0.19 |
| BKN-03 | 0.19±0.32 | -0.06±0.02 | -0.25±0.32 |
| NEEM-EU-08 | -0.61±0.35 | -0.13±0.02 | 0.48±0.35 |
| NEEM-09 | -0.72±0.16 | -0.14±0.02 | 0.58±0.16 |

**Appendix C: Atmospheric reconstruction re-scaled to NEEM-09 and without**

**data re-scaling**


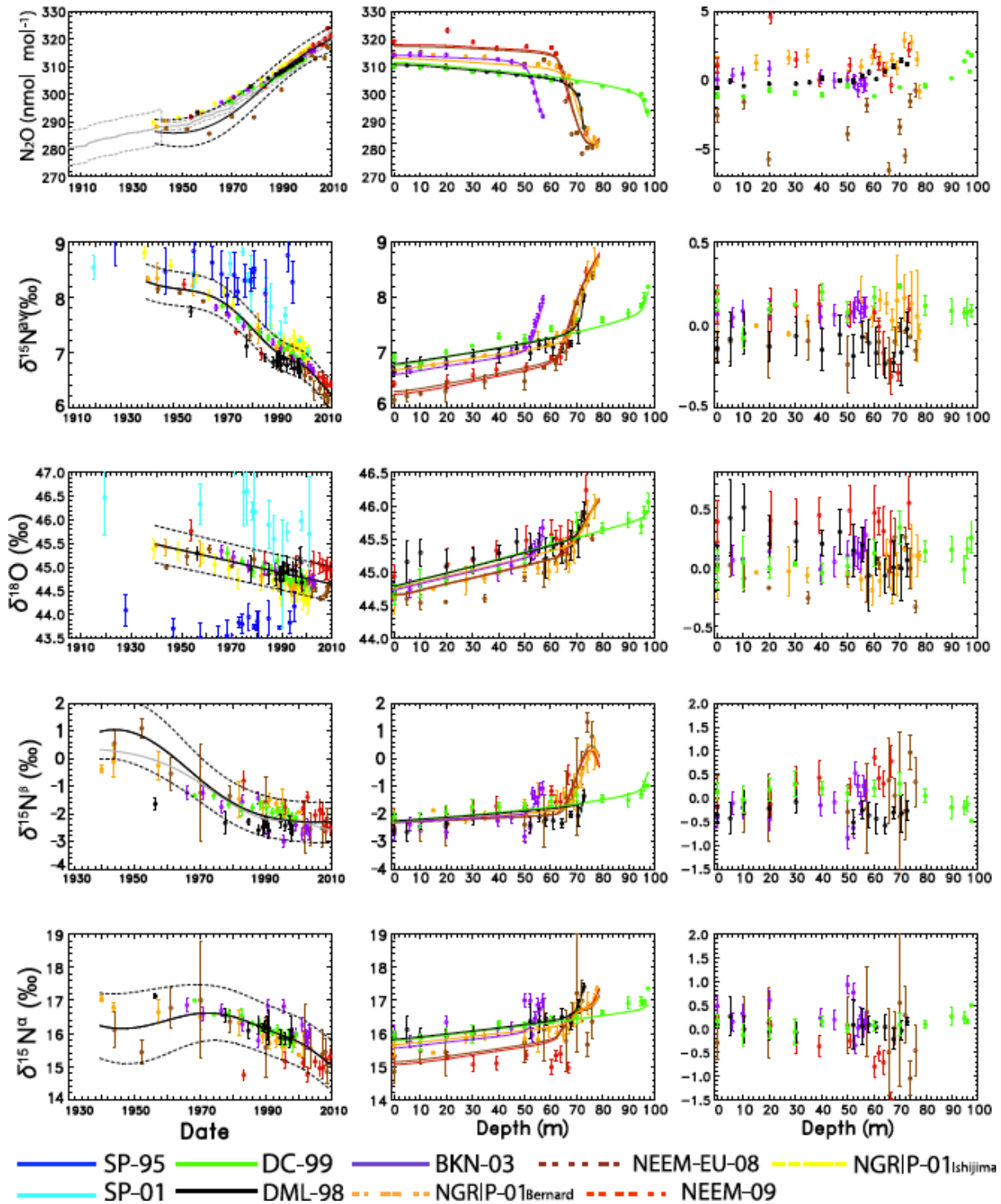
Figure C1. Results of the firn data evaluation (similar to Figure 2) using the data without re-scaling as indicated in the text, Orange: NGRIP-01$_{Bernard}$, Yellow: NGRIP-01$_{Ishijima}$, Brown: NEEM-EU-08, Red: NEEM-09, Purple: BKN-03, Black: DML-98, Green: DC-99, Blue: SP-95 and Light Blue: SP-01.
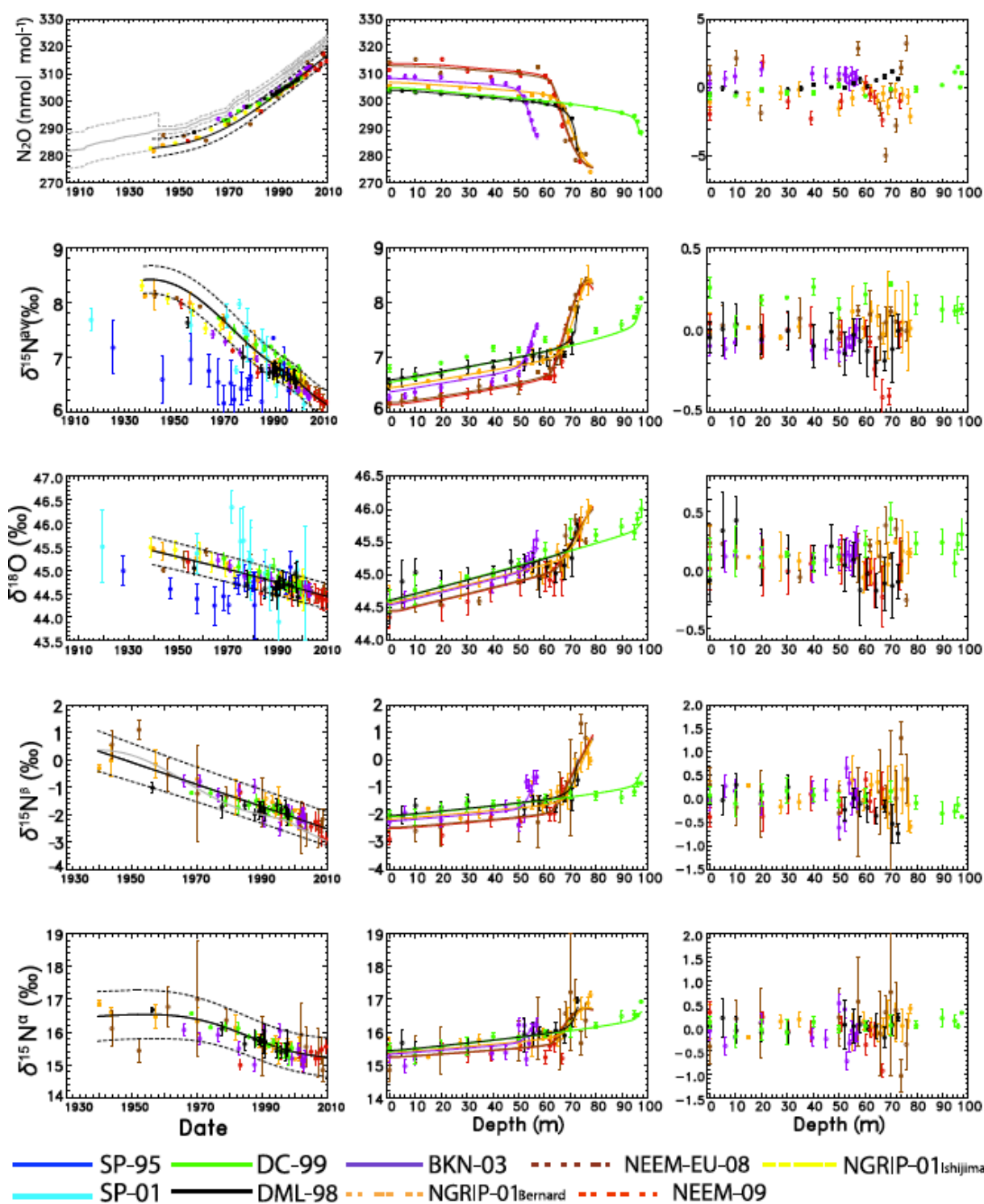
Figure C2. Results of the firn data evaluation (similar to Figure 2) using the data re-scaled to the NEEM-09 site. Colours as in Fig. C1.
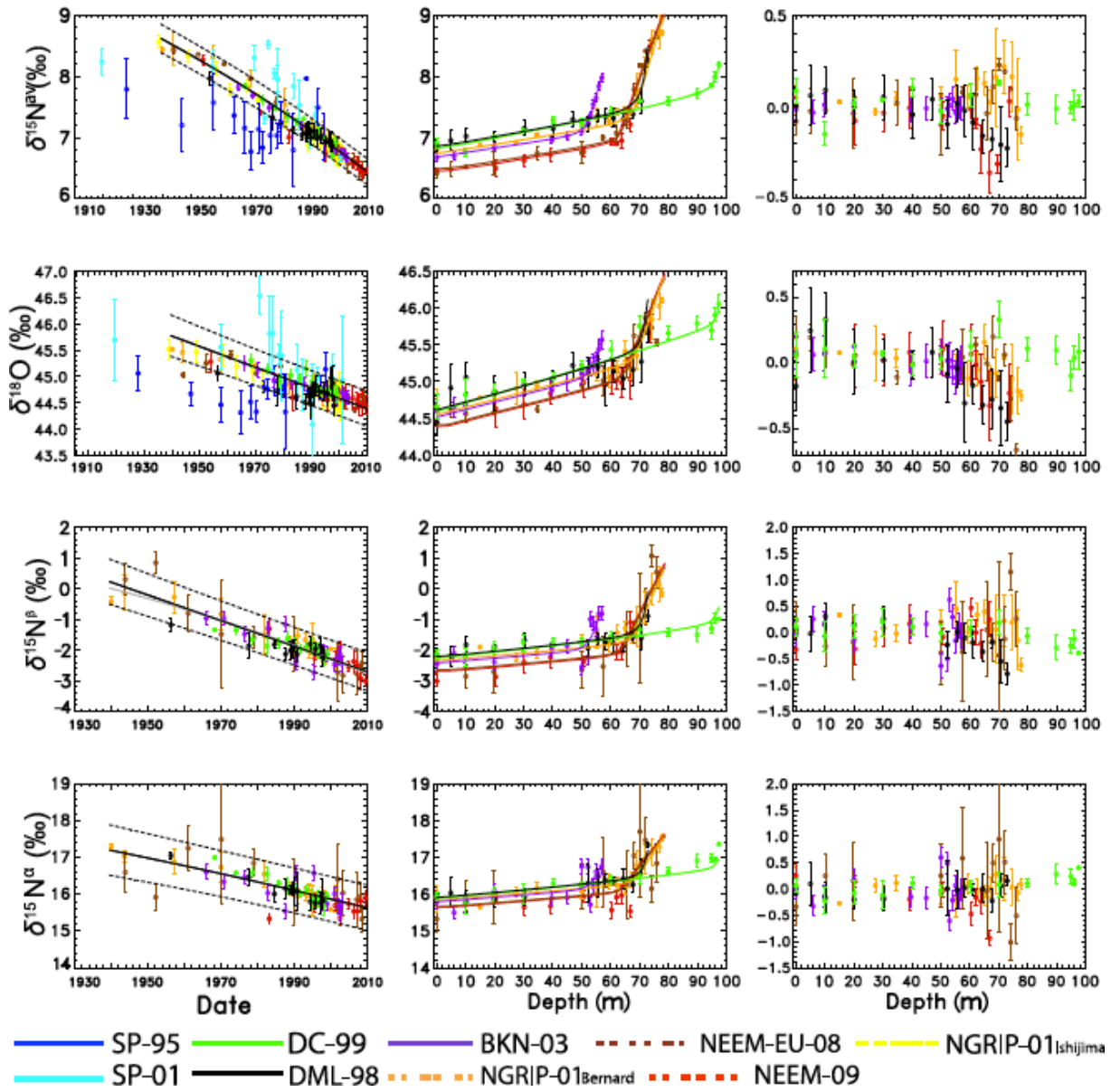
Figure C3. Sensitivity test to the regularization term increased by a factor of 10. Reconstructed atmospheric scenarios (left), corresponding fit of the firn data (centre) and model data discrepancies (right). The best reconstructed scenarios are shown as the black continuous lines, with model derived uncertainties (2σ) in dashed lines. Colours as in Fig. C1.
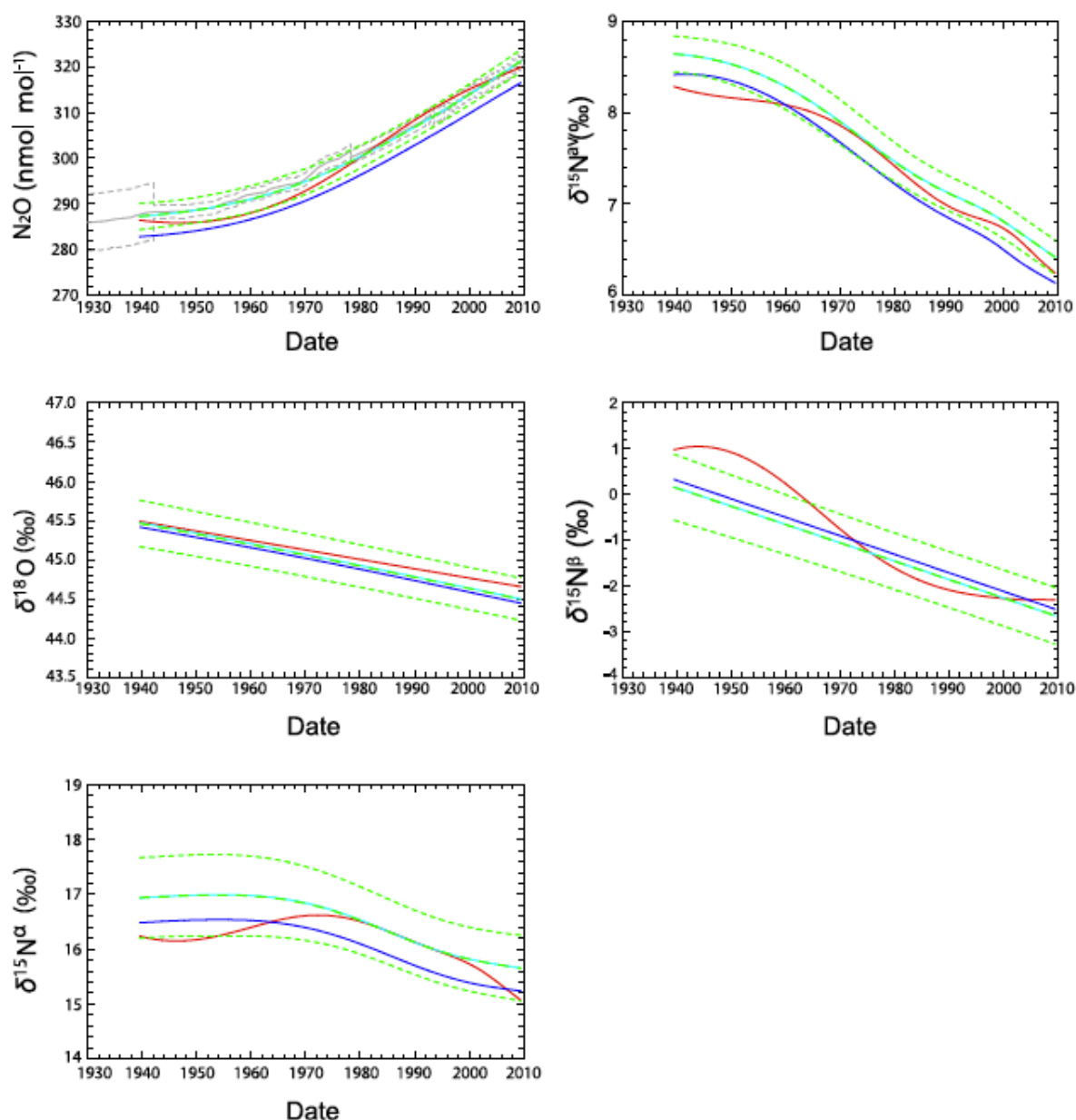
Figure C4. Comparison of the atmospheric reconstructions between different re-scaling methods. Solid and dashed green lines are the scenarios from data re-scaled to DC-99 used in this study. Solid red lines are the best-case scenario for the non re-scaled data and solid blue lines are the best-case scenarios from the data re-scaled to NEEM-09. The latter data series is shifted because of a calibration offset. When this is corrected for the data superimposes the green lines as expected.

**Appendix D: Sensitivity of the reconstructed N$_2$O emissions and isotopic signatures on N$_2$O lifetime.**

For the default calculations with the mass balance model a constant lifetime for N$_2$O was used. A recent study from Prather et al. (2015), though, highlighted that top-down model calculations are sensitive to changes in the N$_2$O lifetime. To quantify the effect on our results we performed a sensitivity test where we linearly changed the N$_2$O lifetime from pre-industrial to modern times from 123 a in 1700 to 119 a in 2008. We also included runs with the absolute mean value changes in the assumed mean lifetime. The results are shown in Figures D1 and D2 below.

In Figure D1 the N$_2$O atmospheric budget is re-calculated and compared with the results when the constant lifetime of 123 a is used. In year 1940 the N$_2$O emissions are (12.3±2.7) Tg a$^{-1}$ N and (17.0±1.7) Tg a$^{-1}$ N in year 2008 with a total increase of (4.7±1.7) Tg a$^{-1}$ N. When keeping the lifetime constant, the results for the same years are (11.9±1.7) Tg a$^{-1}$ N and (16.4±1.7) Tg a$^{-1}$ N with a total increase of (4.5±1.7) Tg a$^{-1}$ N. In addition, when looking also into the absolute mean value changes in the assumed mean lifetime we only observe a vertical shift of the scenarios that do not affect the temporal change. This shows that there is a sensitivity on the choice of lifetime for our mass balance model on the N$_2$O atmospheric budget as was indicated by Prather et al. (2015).

The N$_2$O source isotopic signature shows no significant change with the choice of lifetime giving similar average source values for all source signatures as for when using a constant lifetime of 123 a.

On the other hand, the N$_2$O average anthropogenic source signature displays a sensitivity in the choice of lifetime returning values (−15.9±2.6) ‰, (28.5±2.6) ‰, (−7.2±1.7) ‰ and (−22.8±8.4) ‰ for $\delta^{15}N^{av}$, $\delta^{18}O$, $\delta^{15}N^{\alpha}$ and $\delta^{15}N^{\beta}$ respectively. This agrees within combined errors with the total average values of (−18.2±2.6) ‰, (27.2±2.6) ‰, (−8.1±1.7) ‰ and (−26.1±8.4) ‰ for $\delta^{15}N^{av}$, $\delta^{18}O$, $\delta^{15}N^{\alpha}$ and $\delta^{15}N^{\beta}$ respectively when a constant 123 a lifetime is used. On average, the N$_2$O anthropogenic signature results can differ by 10 % when a different lifetime is chosen, which is equivalent to a (2.0±1.0) ‰ difference in the final anthropogenic values.

Sensitivity tests were also performed on the F$_{exch}$ parameter which gives us the annual fluxes between the two reservoirs (stratosphere - troposphere). Following Appenzeller et al. (1996)

1154    and Holton et al. (1990) the value was tested at a low and high value of 0.16 and 0.28 Tmol s$^{-1}$

1155    respectively with the one used in the manuscript being 0.22 Tmol s$^{-1}$. Results are shown in

1156    figures D3 and D4 below.

1157    In Figure D3 (middle panel) the atmospheric budget is re-calculated and compared to the

1158    optimal scenario values. At the bottom panel the air returned to troposphere from stratosphere

1159    is presented ($F_{exch}$). It is clear that when a low $F_{exch}$ value is chosen, then less $N_2O$ is returned

1160    to the troposphere. Contrary when a higher $F_{exch}$ value is used more $N_2O$ is returned.

1161    $F_{exch}$ choise has little effect on the isotopic signature results as shown in Figure D4 and is

1162    mainly limited to the earliest part of the record (>1970) where the reconstruction uncertainties

1163    are larger. While it is expected when $F_{exch}$ value is low the isotopic results to be more

1164    enriched compared to higher $F_{exch}$, in our case this is not clear from the test. The overal

1165    averaged values have a less than 2 % difference compared to the chosen (optimal) scenario

1166    and results of total averaged source and anthropogenic isotopic signatures are well within

1167    agreement with combined uncertainty errors in both total source and anthropogenic signatures

1168    respectively.

1169    Thus, we conclude that while the flux is indeed sensitive on the $F_{exch}$ choice value the isotopic
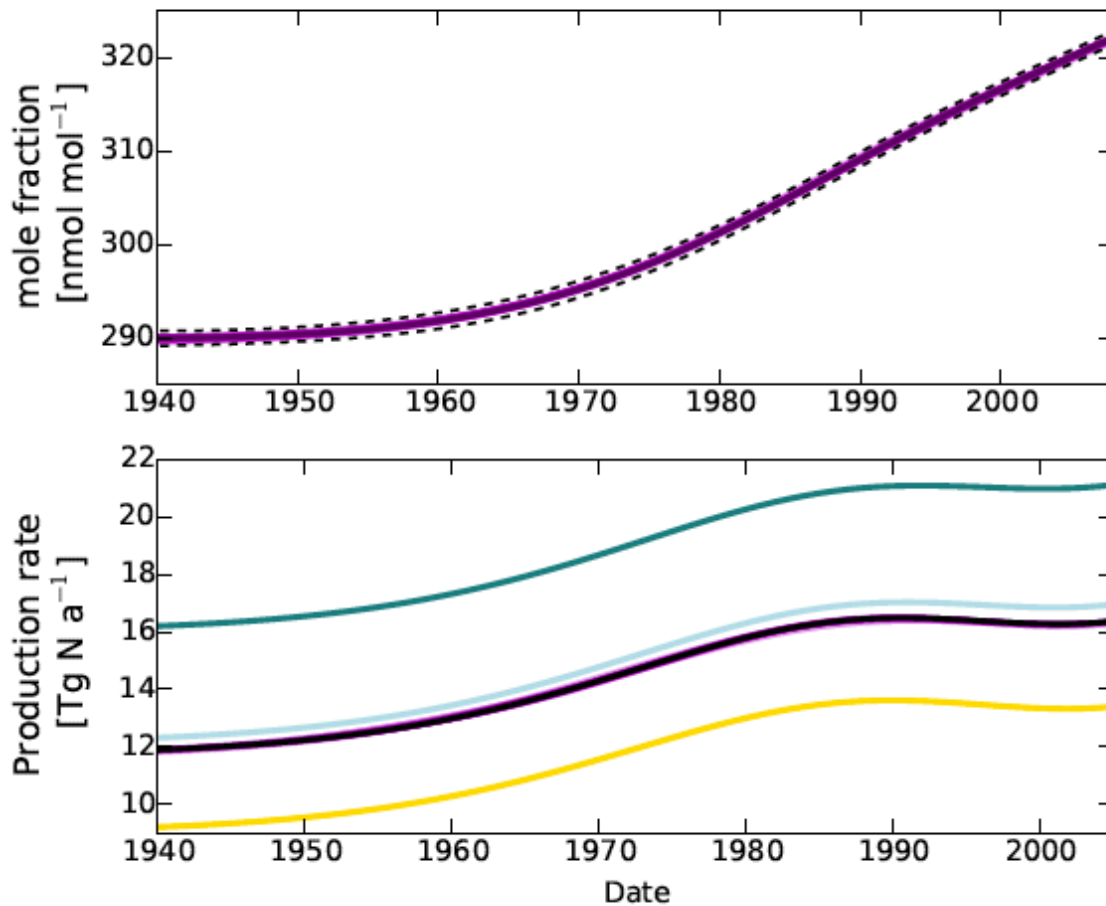
1170    composition is not.

1171
1172  Figure D1: Top panel. $N_2O$ mole fraction history constrained with the most precise data at
1173  NEEM only to narrow the uncertainties (solid black line with uncertainty envelopes as dashed
1174  black lines) and the scenarios within the uncertainty envelopes that were used in the mass
1175  balance model (magenta lines) to evaluate the uncertainties of the atmospheric modelling
1176  results.

1177  Bottom panel. $N_2O$ production rate as calculated from the mass balance model assuming a
1178  change in the lifetime from 123 a in 1700 to 119 a in 2008 (relative change similar to Prather
1179  et al., 2015) in light blue. The solid black line represents the result for the best fit
1180  reconstruction while magenta lines represent the results for the individual scenarios from the
1181  top panel (lifetime kept constant at 123 a) as used in the main paper. Light green and yellow
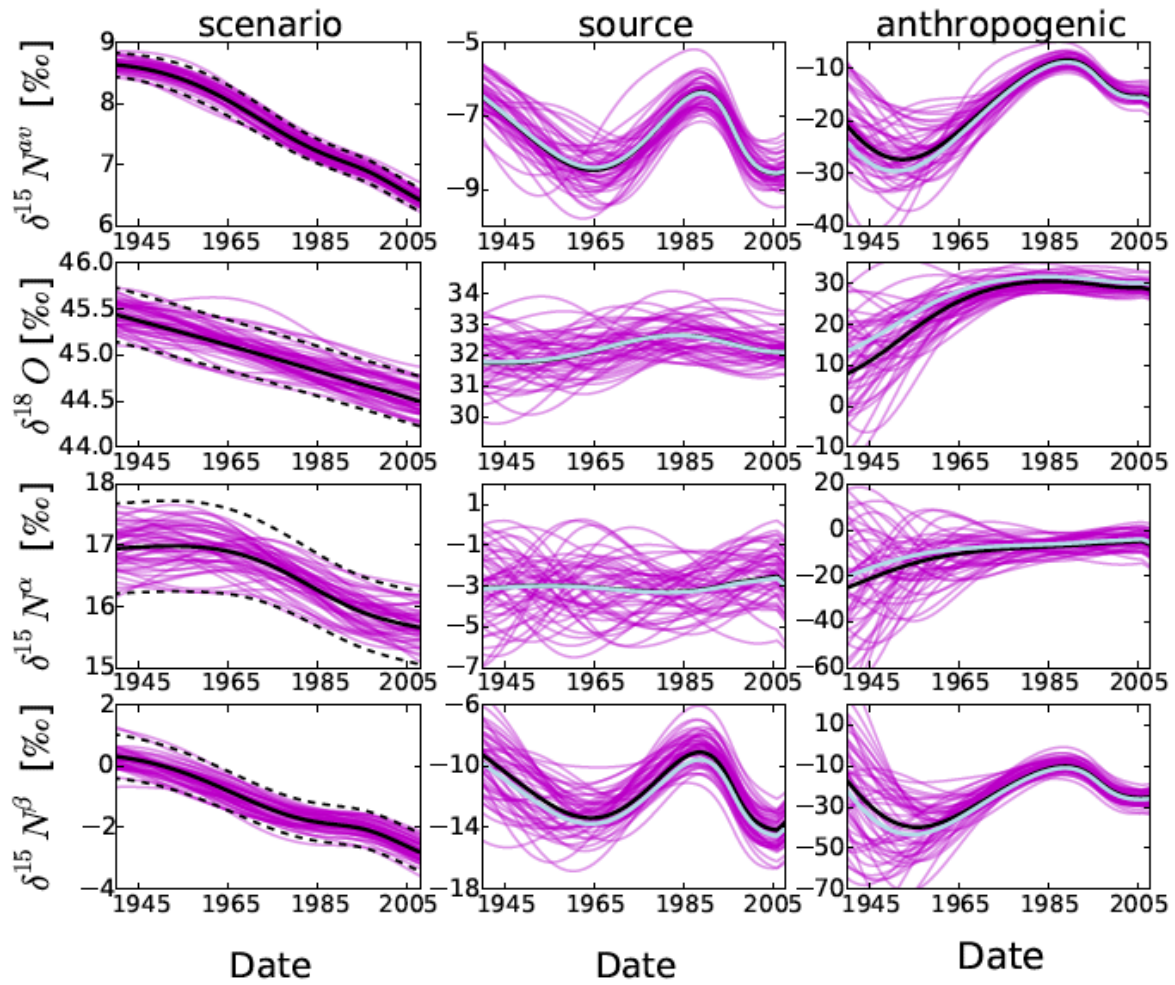1182  show the results when lifetime is 154 a and 104 a  respectively.

1183

1184

1185

Figure D2: Left panels: Historic evolution of $\delta^{15}N^{av}$, $\delta^{18}O$, $\delta^{15}N^\alpha$ and $\delta^{15}N^\beta$ in $N_2O$ as derived from the firn air reconstruction. The solid black line represents the best-fit scenario while the dashed ones represent the respective uncertainties as determined by the reconstruction method. Magenta lines represent the emissions that are required to produce the magenta $N_2O$ histories in the left panels. Middle and right panels: Isotope signatures of the total emitted $N_2O$ and anthropogenic source respectively assuming a change in the lifetime from 123 a in 1700 to 119 a in 2008 (relative change similar to Prather et al., 2015) in light blue. The solid black line represents the result for the best fit reconstruction while magenta lines represent the results for the individual scenarios from the top panel (lifetime kept constant at 123 a) as used in the main paper.
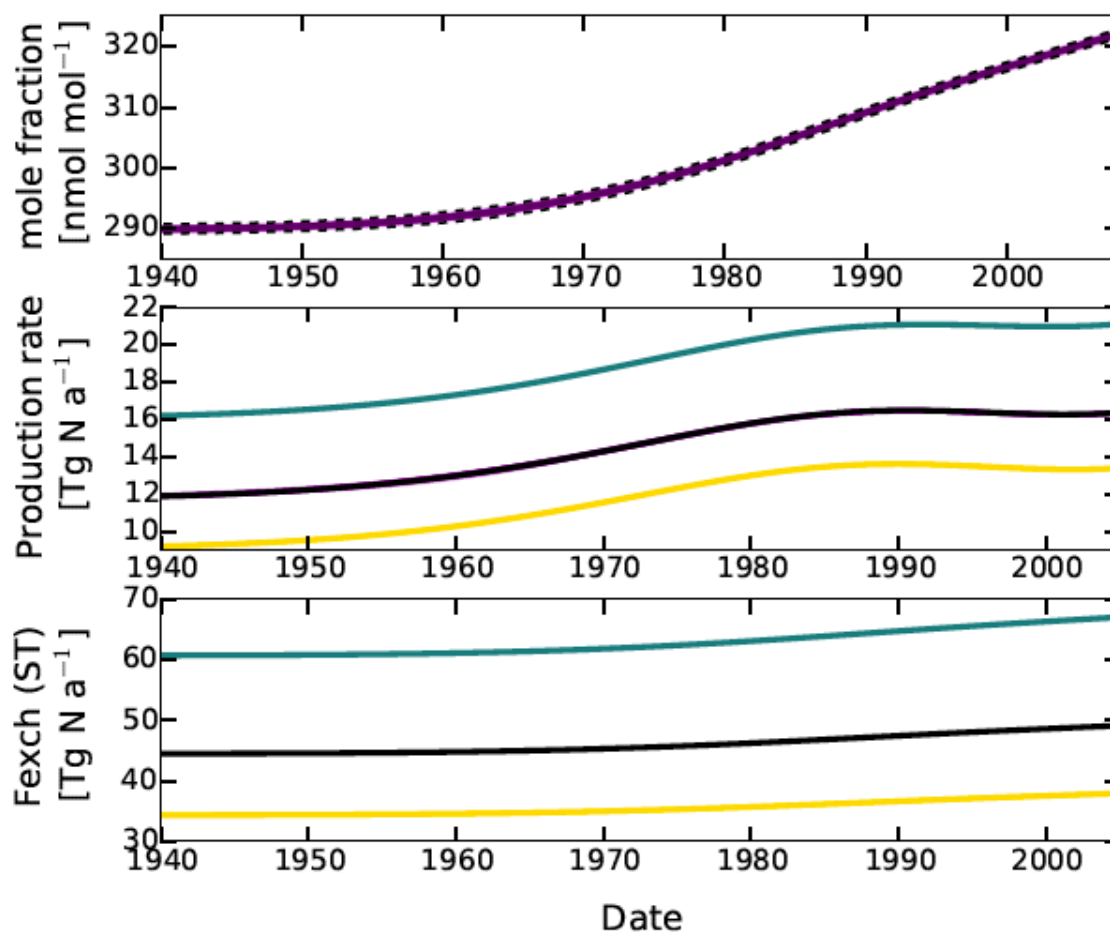
1200

Figure D3: Top panel. $N_2O$ mole fraction history constrained with the most precise data at NEEM only to narrow the uncertainties (solid black line with uncertainty envelopes as dashed black lines) and the scenarios within the uncertainty envelopes that were used in the mass balance model (magenta lines) to evaluate the uncertainties of the atmospheric modelling results.

Middle panel. $N_2O$ production rate as calculated from the mass balance model assuming a high (0.28 Tmol $s^{-1}$) $F_{exch}$ in light green and a low (0.16 Tmol $s^{-1}$) value in yellow. The solid black line represents the result for the best fit reconstruction while magenta lines represent the results for the individual scenarios from the top panel as used in the main paper.

Bottom panel. $N_2O$ flux exchange results between stratosphere and troposphere as calculated from the mass balance model assuming a high (0.28 Tmol $s^{-1}$) $F_{exch}$ in light green and a low (0.16 Tmol $s^{-1}$) value in yellow. The solid black line represents the result for the best fit reconstruction as used in the main paper.

1214

1215
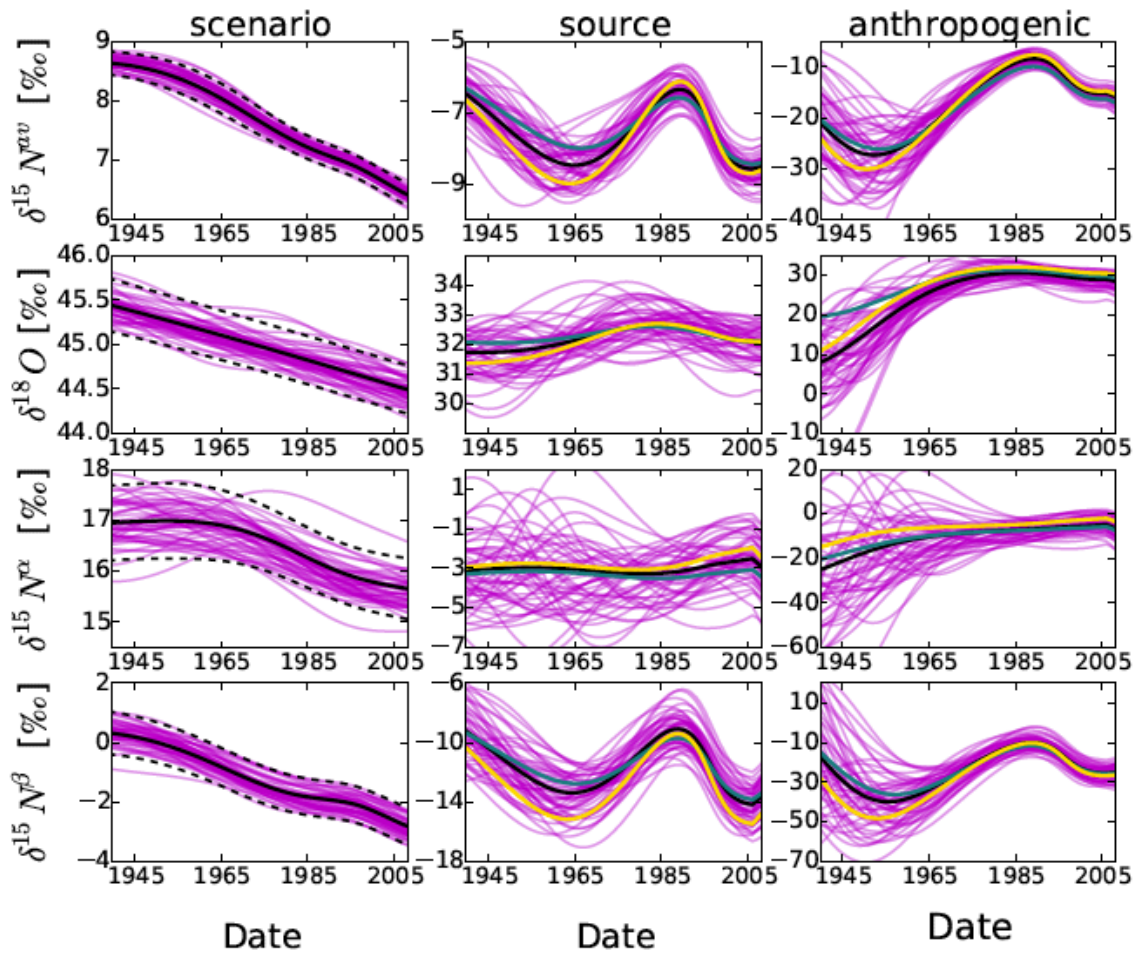


1216

1217 Figure D4: Left panels: Historic evolution of $\delta^{15}N^{av}$, $\delta^{18}O$, $\delta^{15}N^{\alpha}$ and $\delta^{15}N^{\beta}$ in N$_2$O as derived

1218     from the firn air reconstruction. The solid black line represents the best-fit scenario while the

1219     dashed ones represent the respective uncertainties as determined by the reconstruction

1220     method. Magenta lines represent the emissions that are required to produce the magenta N$_2$O

1221     histories in the left panels. Middle and right panels: Isotope signatures of the total emitted

1222     N$_2$O and anthropogenic source respectively assuming high (0.28 Tmol s$^{-1}$) F$_{exch}$ in light green

1223     and a low (0.16 Tmol s$^{-1}$) value in yellow. The solid black line represents the result for the

1224     best fit reconstruction while magenta lines represent the results for the individual scenarios

1225     from the top as used in the main paper.